공학박사 학위논문

Enhancement of electrochemical performance of manganese oxide via coating of electrical conductive materials

전도성 물질 코팅을 통한 망간산화물의 전기화학적 성능향상

2019 년 8 월

서울대학교 대학원

화학생물공학부

고 인 환

Abstract

Enhancement of electrochemical performance of manganese oxide via coating of electrical conductive materials

In-Hwan Ko

School of Chemical and Biological Engineering

The Graduate School

Seoul National University

Lithium ion batteries (LIBs) which currently dominate the market of power sources for portable electronics have been playing an important role for the last three decades. LIBs technology faces emerging demands for the new market of energy requires massive stationary electrical storage and for transportation. To keep pace with market demands, commercial LIBs is demanding improved electrochemical performance such as higher energy density and higher power.

Compared with conventional graphite materials, transition metal oxide materials based on conversion reaction mechanism have shown high reversible capacity. However, their practical applications have been prevented by a poor cycle life caused by volume changes and its low conductivity. The past decade has witnessed

tremendous advances in preparation of nanostructured transition metal oxides for conversion reaction anodes. The advances have been made through morphology control, and carbon-based composite nanostructures synthesis.

The overview of LIBs is introduced in chapter 1 including the basic principle. In addition, lithium ion storage in anode materials categorized into three types according to their mechanism, 1) intercalation 2) alloying reaction 3) conversion reactions are also introduced. At the end of this chapter, the studies on abnormal capacities essentially involving conversion reactions are introduced.

In chapter 2, a new composite of Mn_2O_3 nanowires and Poly(3,4-ethylenedioxythiophene) polystyrene sulfonate (PEDOT:PSS). PEDOT:PSS is a conductive polymer mixture was prepared. In order To overcome capacity fading during cycling in conversion reaction of Mn_2O_3, PEDOT:PSS have been added to Mn_2O_3 nanowires. PEDOT:PSS was successfully coated onto Mn_2O_3 nanowires while maintaining the structure of Mn_2O_3. The coating of PEDOT:PSS reduced the resistance of the surface and protected the surface electron channels from the pulverization effect of the charge–discharge operation. α-Mn_2O_3/PEDOT:PSS showed excellent cyclability with a reversible capacity of 1450 $mAh \cdot g^{-1}$ after 200 cycles at a current density of 100 $mA \cdot g^{-1}$. An increase in capacity was observed with continuous cycling, which may be attributed to further oxidation of the manganese species and a reversible reaction of the gel-like polymer on the manganese surface. The results demonstrate that PEDOT:PSS enhances the electrochemical activity by providing electron channels and prevents pulverization caused by the charge and discharge process.

In chapter 3, Compared with conventional graphite materials, transition metal

oxide materials based on conversion reaction have shown high reversible capacity. However, their practical applications have been prevented by a poor cycle life caused by volume changes and its low conductivity. The past decade has witnessed tremendous advances in the preparation of nanostructured transition metal oxides for conversion reaction anodes. Peapod-like nanowires with a carbon coating layer showed excellent performance among the investigated composites to overcome the obstacles. Herein, the principle of forming the peapod-like nanowires is presented, and the improved composite with well-disposed MnO particles in the core is synthesized. The morphology of the manganese oxide particles inside the carbon layer could be controlled by adjusting the parameters in the carbonization process. The improved composite showed steady cycling performance without decreasing the capacity, and the rate performance was outstanding. The improved structure can maximize the advantages such as structural durability against the stress involving volume changes and minimizing the side reaction at the surface.

Keywords: lithium ion batteries, anodes, conversion reaction, manganese oxide, conductive polymer, core-shell MnO/C

Student number: 2012-30741

List of Tables

List of Figure

Contents

Chapter 1. Introduction

1.1 Basic principles of lithium ion batteries

Lithium-ion battery is a type of secondary battery, i.e. rechargeable battery, which is an electrical energy storage with high energy density. Due to their extremely high energy density, lithium-ion batteries are widely used for portable electronic devices, such as laptop computers, smartphones, electric vehicles, and so on. Lithium-ion battery is operated by the lithium-ion movement between the negative and positive electrodes inducing the electrochemical reactions in the electrode materials, which converts the electrical energy into the chemical energy and vice versa for the electrical energy storage and usage, respectively [1-3]. The schematic illustration of the lithium-ion battery working principle is shown in Figure 1.1 [4]. A lithium-ion battery cell is composed of positive electrode (cathode), negative electrode (anode), electrolyte, and separator. Lithium ions move toward the negative or the positive electrode through the electrolyte (generally with liquid phase) and electrons are also transferred toward the same electrode with lithium ions through external circuit. Electrons should not be transferred through the electrolytes not to cause a short circuit. For this reason, the electrolyte materials must be ionic conductor, but electronic insulator. Additionally, the separator is laid between the negative and positive electrodes, which also protects from the short circuit by physically separating the two electrodes. The negative and the positive electrodes are directly related to the electrochemical reaction, which operates the lithium-ion batteries. When lithium ions are transferred into the electrode material, electrons are also transferred into the electrode material through the external circuit at the same time,

which leads to the electrochemical reaction of the electrode material and the energy conversion between the electrical and the chemical energies. During the electrochemical reaction in the lithium-ion battery, it is generally known that oxidation or reduction occurs in the host material instead of the lithium ions. The solid state materials that can accept lithium ions can be either of cathode or anode materials depending on the relative lithium stability in the host material, i.e. lithium chemical potential [1]. When two electrode materials are set up in the lithium-ion battery, the one in which lithium ions settle down more stable (lower chemical potential of lithium) is classified as the cathode material. Discharging occurs by the spontaneous movement of lithium ions in the closed circuit from anode (higher Li chemical potential) to cathode (lower Li chemical potential), which is driven by Li chemical potential gradient between two electrodes. The stored electrical energy from anode is used for the operation of electronic devices during the discharge procedure. On the contrary, charging process can occur by the external electric force that compels the electrons to move toward the anode side, which causes the lithium insertion into the anode and the electrical energy storage of the lithium-ion battery [2]. The energy density (volumetric or gravimetric) of lithium-ion battery is determined by the combination of the cell voltage and the specific (or volumetric) capacity. The cell voltage can be roughly calculated by the average potential difference between the anode and cathode. The specific (or volumetric) capacity indicates the available charge amount per unit weight (or volume). In general, the high specific capacity greatly contributes to the high energy density of lithium-ion batteries. The conventional cathode and anode materials, lithium cobalt oxide ($LiCoO_2$) and graphite (C_6), show the specific capacity of ~135 mAh/g and ~370

mAh/g in the practical voltage range; they result in the specific energy density of 140 Wh/kg, which is much higher than the previous NiMH battery, 75 Wh/kg [3].

1.2 Cathode materials

The cathode is one of the important components of LIBs. The cathode material must have a stable crystalline over wide ranges of composition because during the charging cycle, the oxidation reaction leads to large compositional changes and therefore to unfavorable phase changes [5]. Finding the right material with the required structural stability is a great challenge. During discharging cycle, lithium ions are transported back into the cathode material and a reduction of the transition metal ions in the cathode is carried out by the electrons from the anode. The maximum discharge current is controlled by the rates of these two processes, as well as access of the lithium ions in the electrolyte to the electrode surface. Cathode performance directly depends on the electrode microstructure and morphology, as well as the inherent electrochemical properties of the cathode material since lithium ion exchange with the electrolyte only happens at the electrode–electrolyte interface [6, 7]. Cathode materials can store energy through two different mechanism, (1) intercalation and (2) conversion reaction [7]. Conversion electrodes undergo a solid-state redox reaction during lithiation/delithiation, in which there is a change in the crystalline structure, accompanied by the breaking and recombining chemical bonds, while the intercalation cathode materials act as a host for Li ions, so that the ions can insert in or extract from the material reversibly. Metal halides such as FeF_2, CoFe, NiF_2 are examples of conversion based cathode materials. Due to the large volume expansion, poor electron conductivity and hysteresis issues, development of

conversion based cathode materials has faced a lot of challenges [7]. Intercalation based cathode materials are mainly divided into three categories: chalcogenides, transition metal oxides and polyanion compounds. Most of research on intercalation cathode materials is focused on transition metal oxides due to their higher operating voltage and the resulting higher energy storage capability [7]. $LiCoO_2$ is the most commonly used cathode material in lithium ion batteries. The cathode reaction is represented as follows [6]: $LiCoO_2 \leftrightarrow 1/2\ Li+ + 1/2e^- + Li_{0.5}CoO_2$. The maximum potential resulting from the removal of lithium from $LiCoO_2$ is roughly 4.2 V (vs. $Li/Li^{+)}$, which means that at most 140 mAh g^{-1} of the cathode capacity which is about half of its theoretical capacity, is used in the phase transition between $LiCoO_2$ and $Li_{0.5}CoO_2$. The major benefit of these Li-ion batteries compared to lithium metal-based batteries is relying on the cathode material as the source of lithium which has resulted in exceptional safety features and a guaranteed longer shelf life [8, 9]. However, LCO cannot be used as cathode material in relatively large batteries due to its high cost of cobalt and safety issues [10]. Therefore, newer and better materials are constantly developed to lower cost and improve stability. Another class of cathode materials are spinel oxides with AB_2O_4 formula. The most famous in this group is $LiMn_2O_4$ (LMO). The spinel structure creates a three-dimensional framework which promotes the movement of lithium ions [8, 11]. LMO delivers a possible capacity at 100 to 120 mAh g^{-1} (with a theoretical specific capacity of 148 mAh g^{-1}); but, its reversible capacity is less than that of LCO or LNO. A unique advantage of LMO is that it's spinel structure undergoes less damage during charging/discharging cycles in comparison with the layered structure because the continuous two-way transportation of lithium ions in the spinel structure does not

make a large volume change at room temperature. On the other hand, at high temperatures LMO shows poor life characteristics of both cycle and calendar life [8]. Even though LMO is reliable and relatively cheap to produce, its low capacity does not permit it to be used as a single cathode material. On the other hand, the layered structure of NMC has a higher capacity and hence, the cathode material in the new generation of commercially produced batteries consists of a complementary blend of LMO and NMC [12].

Olivine $LiFePO_4$ (LFP) is poly anionic compound that has attracted a lot of attentions due to their thermal stability and high-power capabilities. In LFP, the release of oxygen from the active cathode material is inhibited due to the strong P-O bond in phosphate even in harsh environments [13, 14]. LFPs are structurally stable which helps guarantee their safety. Also, the low cost and their environmentally friendly nature support their position as a potential candidate for cathode materials in electric vehicles [8].

1.3 Anode materials

Three different reaction mechanism of anode materials are shown in Figure 1.2. Graphite is the best representative material in insertion group of anode materials. Lithium ions in graphite are electrochemically intercalated into the space between the layers of materials. Lithium ion intercalation in graphite can be described as follows: $xLi^+ + C_6 + xe^- \leftrightarrow Li_xC_6$. Graphite in its natural or artificial form has been widely used in LIBs for mobile devices. The reversible lithiation/delithiation reaction proceeds less than 0.25 V versus Li/Li^+, with a practical reversible capacity greater than 360 mAh g^{-1} (theoretically at 372 mAh g^{-1} or 975 mAh cm^{-3}) with high

discharge/charge efficiency approaching 100% [15, 16]. However, one downside is that some irreversible reactions during the first charge (lithiation) process cause a cathodic decomposition of a number of constituents of the electrolyte. For example, ethylene carbonate, the most conventional solvent of electrolytes for LIBs, is decomposed between 0.5 V and 0.7 V to form a passive layer on the surface of graphite [8]. Practically, an efficiency greater than 90% of discharge to charge has been recorded at the first cycle with the initial capacity of 390 $mAhg^{-1}$. Charge/discharge reversibility which is essential for long-term cycle-ability is achieved after a stable passive layer called the solid-electrolyte interface (SEI) layer is formed. Therefore, the properties of the SEI layer should be well-known, as this layer is crucial to the performance and stability of battery cells. The SEI layer should be electrically insulating to prevent any further electron transfer from the electrode to the electrolyte hindering any additional decomposition of the electrolyte material after the formation of the SEI layer. On the other hand, the SEI layer should be ionically (especially with respect to Li^+ ions) conductive, enabling the mass transfer of Li^+ from electrolyte to the interlayer spaces of graphite [17]. A major drawback of graphite anodes is their low capacity. Therefore, efforts have been made for developing other carbonaceous materials to obtain better performance. Increasing the surface area of the carbonaceous materials can provide more space for Li ions accommodation between the layers and therefore higher attainable capacity. New carbon materials such as carbon nanofibers (CNF), carbon nanotubes (CNT) and graphene are vastly studied as an alternative to graphite due to their larger surface area as well as higher electron conductivity which makes them suitable for high rate charging/discharging [18]. Single wall CNTs are expected to exhibit reversible

capacities somewhere around 300–600 mAh g^{-1} [19].

The second most popular anode materials after graphite is the alloying reaction-based materials. This group consists of metals that can be alloyed with lithium such as silicon (Si), germanium (Ge), tin (Sn) and their alloys as shown in figure 1.3 [2,15, 20, 21]. In alloying reactions, the Li ions insert into the structure of anode material during the charge cycle, making an alloy with the anode. The reversible alloying reaction is shown as follows: $M + xLi^+ + xe^- \leftrightarrow Li_xM$, where M is the anode material. If the Li has a good solubility in the host material, a solid solution is made. But If the solubility of Li in the host anode material, is limited, alloying may result in phase change, meaning that Li_xM has a different phase structure than pure M. Therefore, both alloying/de-alloying reaction and phase change may take place in the anode material during charge/discharge. The alloying-de-alloying mechanism in Si, Sn, Al and Sb is accompanied with phase change [22]. Alloying reaction-based materials are most famous for their high theoretical capacity: 4200 mA h g^{-1} for Si in $Li_{4.4}Si$, 1600 mA h g^{-1} for Ge in $Li_{4.4}Ge$, 993 mA h g^{-1} for Al in LiAl, 992 mA h g^{-1} for Sn in $Li_{4.4}Sn$ and 660 mA h g^{-1} for Sb in Li_3Sb [23]. However, the major disadvantage of these materials is their extremely large volume change during charge and discharge [19]. They experience serious pulverization resulting in electrical isolation of the active materials from electric contact with carbon black and the current collector. Among the alloying elements which can be used in this group of anode materials, most of the research and development has been focused on silicon because of its highest capacity and low voltage [19].

Conversion reaction based materials are the last group of anode materials, not being practically used and being studied only. Conversion reaction based materials are

based on the faradaic reaction represented as follow: MaXb + (b,n) Li+ + ae- aM + bLinX , where M=transition metal (such as Ti, V, Cr, Mn, Fe, Co, Ni, Cu, Mo, W, Ru), X=anion (such as O, N, F, S and P) and n=number of negative charge of X [24]. A variety of anode materials are possible in this group by a simple combination of candidates of M and X even without considering multiple oxidation states of M. The theoretical capacity of the conversion-reaction-based anode materials range from the low range of 350 mAhg-1 for Cu2S to the high range of 1800 mAh g^{-1} for MnP4 [24]. The relatively high theoretical capacity of conversion-reaction-based compounds as compared to graphite (372 mAhg-1) makes these materials as ideal anode materials. However, these materials have some major drawbacks which must be dealt with before being used as anode material. Firstly, their discharge to charge efficiency is not as good as that of graphite which drastically decreases their cycle-ability. This means that the conversion reactions in conversion-reaction-based anodes would have intrinsically limited reversibility. Secondly, large volume changes of the conversion-reaction-based anode materials during lithiation and the following delithiation could lead to pulverization or electric isolation [25, 26]. Thirdly, the reaction potentials of conversion-reaction-based anode materials (E_{conv}), at which the potential profiles reach a plateau, are relatively higher than that of graphite. Higher E_{conv} leads to lower cell potential which results in a lower energy density than expected only from capacities [24].

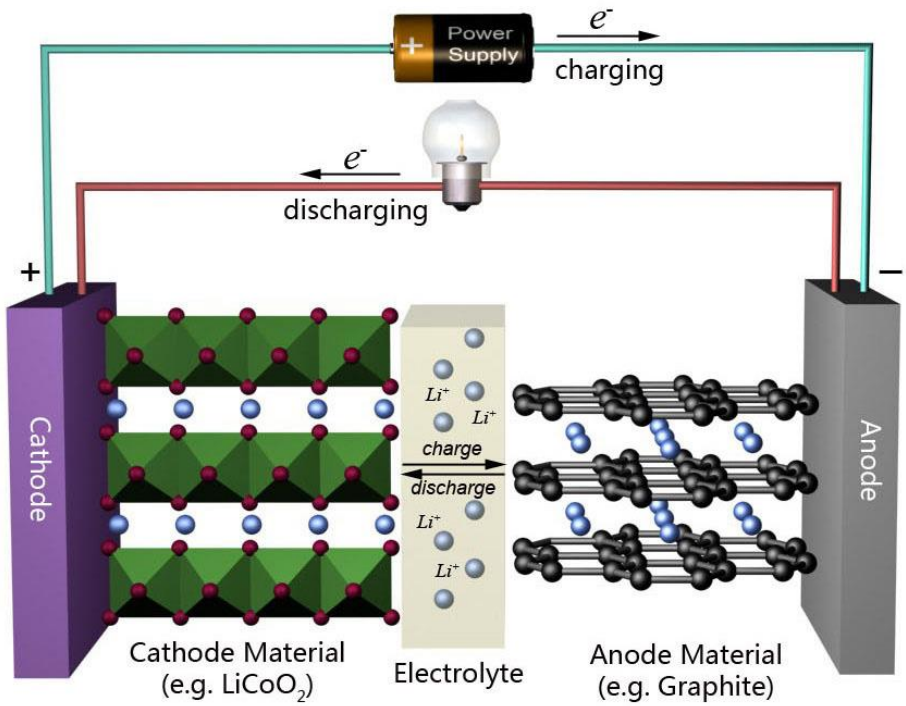

Fig. 1. 1 Schematic illustration of the lithium ion batteries. Adapted from Ref [4] (R. Liu, J. Duay, S.B. Lee, Chemical Communications, 47 (2011) 1384-1404).

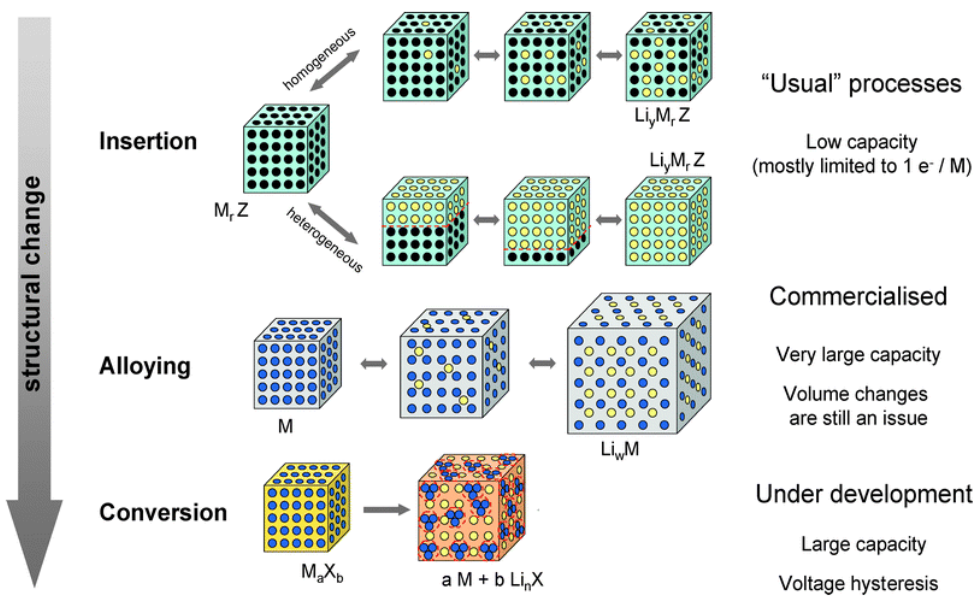

Fig. 1. 2 A schematic representation of the different reaction mechanisms observed in electrode materials for lithium batteries. Black circles: voids in the crystal structure, blue circles: metal, yellow circles: lithium. Adapted from Ref [2] (M.R. Palacin, Chemical Society Reviews, 38 (2009) 2565-2575).

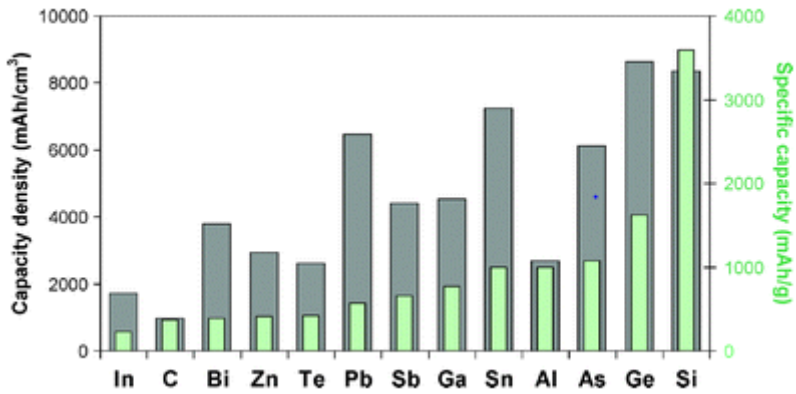

Fig. 1. 3 Specific capacities and capacity densities for selected alloying reactions. Values for graphite are given as a reference. Adapted from Ref [2] (M.R. Palacin, Chemical Society Reviews, 38 (2009) 2565-2575).

1.4 The extra capacity in metal oxide reacting through conversion reaction

The discovery that a series of metal salts (typically oxides and fluorides, MF_x and M_xO_y could reversibly react with lithium through a conversion-type reaction where the metal salt is lithiated to form a composite structure comprising metal particles embedded in a lithium salt [24, 27-34]. An intriguing aspect in the reaction of these systems, which has provoked much debate, is the additional reversible capacity shown beyond the theoretical capacity estimated on the basis the reduction of the metal cation to M^0 [24]. In 2002, this phenomenon was studied in M_xO_y/Li cells [36] by using transmission electron microscopy, and a 'polymer/gel-like film' was observed to form at the grain boundaries between nanoparticles at low voltages (1.9–0.0V). The extra capacity was maintained for 800 cycles [36]. Clare P. Grey et al. used a variety of structural characterization technique (NMR, XRD, PDF, XAS, etc.) to investigate the mechanism for charge storage. The results (figure 1.4) show that a major source of the additional capacity arises from the reversible reaction of LiOH to form LiH and SEI formation [37]. Moreover, the presence of LiOH was suggested as a partly contributor to additional capacity of SnO_2 anode [38]. Recently, the reversible formation and decomposition of SEI layer on carbonaceous materials are reported (figure 1.5) [39]. The reversible SEI layers on hard carbon seems to be similar layers to those observed on conversion-based materials.

In contrast, it was argued on the basis of investigations first on RuO_2 [30] and then more generally on a range of fluorides and oxides [32,33,40–42] that a source of the additional capacity lies in the formation of a so-called space charge layer comprising

Li^+ ions at the interface between the metal and lithium salt particles, charge compensated by additional electrons on the metal surface. These findings have spurred many discussions over the past 15 years [40,42-44], because of the intriguing possibility that the mechanism provides a more general approach for storing charge. At the key reason of the debate lies the experimental difficulty in identifying the structures present at the buried metal/salt interfaces.

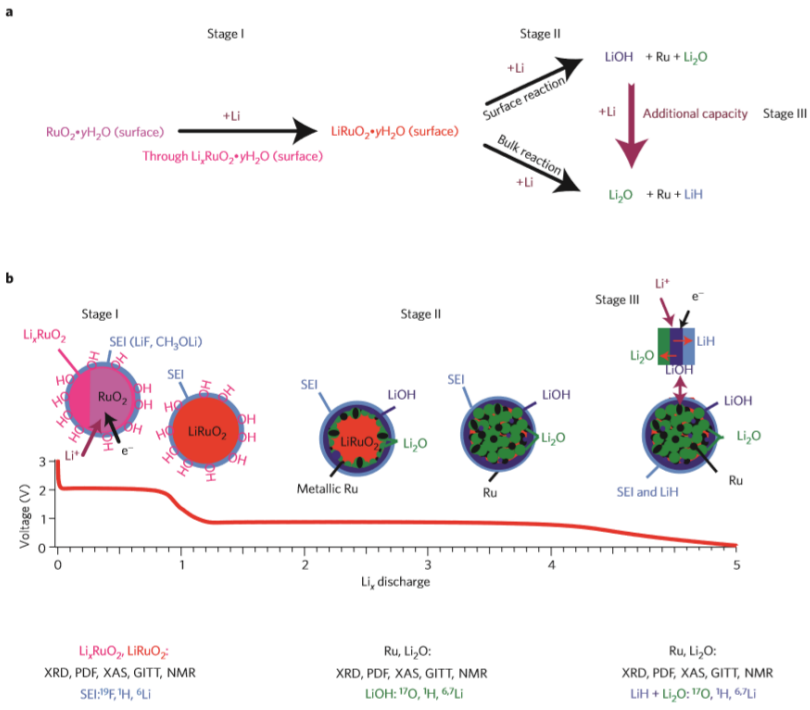

Fig. 1. 4 Summary of the experimental evidence of the RuO2/Li battery system. a, Summarized reaction pathway. b, The profile of the electrochemistry with schematics representing the phase distribution at each stage of discharge. The relevant supporting evidence is given below. GITT, galvanostatic intermittent titration technique. Adapted from Ref [37]

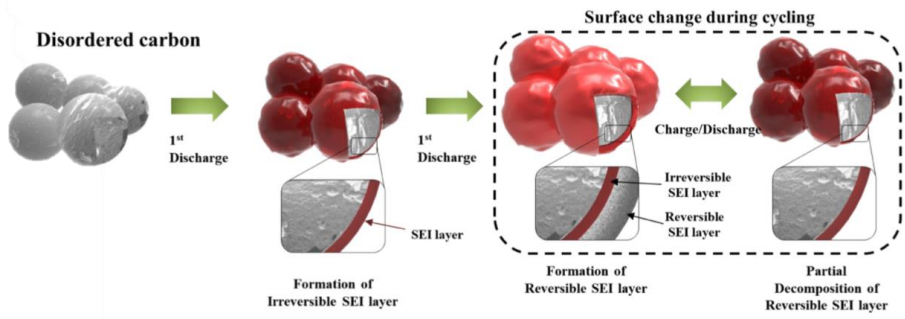

Fig. 1. 5 Schematic illustration of SEI layer formation and decomposition mechanisms of disordered carbon. Adapted from Ref [39]

1.5 Reference

[1] M.S. Whittingham, Chemical reviews, 104 (2004) 4271-4302.

[2] M.R. Palacin, Chemical Society Reviews, 38 (2009) 2565-2575.

[3] G.E. Blomgren, Journal of The Electrochemical Society, 164 (2017) A5019-A5025.

[4] R. Liu, J. Duay, S.B. Lee, Chemical Communications, 47 (2011) 1384-1404.

[5] . Goodenough JB, Park K, The Li-Ion Rechargeable Battery : A Perspective, 2013;

[6] Etacheri V, Marom R, Elazari R, Salitra G, Aurbach D, Energy & Environmental Science, 4 (2011) 3243.

[7] Porosoff M.D., Kattel S., Li W., Liu P., Chen J.G., Chemical Communications, 51 (2015) 6988–6991.

[8] Kim T-H, Park J-S, Chang SK, Choi S, Ryu JH, et al., Advanced Energy Materials, 2012; 2 (2012) 860–872.

[9] Fergus JW, Journal of Power Sources, 195 (2010) 939–954.

[10]Shaju KM, Subba Rao G V, Chowdari B.V.R., Electrochimica Acta, 48 (2002) 145–151.

[11] Park OK, Cho Y, Lee S, Yoo H-C, Song H-K, et al., Energy & Environmental Science, 4 (2011) 1621.

[12] Myung S-.T., Maglia F., Park K-.J., Yoon C.S., Lamp P., et al., ACS Energy Letters, 2 (2017) 196–223.

[13] Yamada A., Chung S.C., Hinokuma K., , Journal of The Electrochemical Society, 148 (2001) A224.

[14] Huang Z-.D., Oh S-.W., He Y-.B., Zhang B., Yang Y., et al., Journal of Materials Chemistry, 22 (2012) 19643.

[15] Goriparti S., Miele E., De Angelis F., Di Fabrizio E., Proietti Zaccaria R., et al., Journal of Power Sources, 257 (2014) 421–443.

[16] Liu Y., Wang Y.M., Yakobson B.I., Wood B.C., Physical Review Letters, 113 (2014) 28304.

[17] Verma P., Maire P., Novák P., Electrochimica Acta, 55 (2010) 6332–6341.

[18] Raccichini R., Varzi A., Passerini S., Scrosati B., Nature Materials, 14 (2015) 271–279.

[19] Liu C., Li F., Ma L-.P., Cheng H-.M, Advanced Materials, 22 (2010) 28-62.

[20] Su X., Wu Q., Li J., Xiao X., Lott A., et al., Advanced Energy Materials, 4 (2014)1300882.

[21] Wang B., Luo B., Li X., Zhi L., Materials Today, 15 (2012) 544–552.

[22] Obrovac M.N., Chevrier V.L., Chem. Rev., 114 (2014) 11444–11502.

[23] Yoo H., Lee J., Kim H., Lee J., Cho J., et al., Nano Letters 11 (2011) 4324–4328.

[24] Cabana J., Monconduit L., Larcher D., Palacín M.R., Advanced Materials, 22 (2010) 170-92.

[25] Dong X., Li L., Zhao C., Liu H., et al., Journal of Materials Chemistry A, 2 (2014) 9844–9850.

[26] Zhou W., Zhu J., Cheng C., Liu J., Yang H., et al., Energy & Environmental Science, 4 (2011) 4954–4961.

[27] Idota, Y., Kubota, T., Matsufuji, A., Maekawa, Y. & Miyasaka, T. Science 276 (1997) 1395–1397.

[28] Poizot P., Laruelle S., Grugeon S., Dupont L. & Tarascon J. M., Nature 407 (2000) 496–499.

[29] Amatucci G. G. & Pereira N., J. Fluor. Chem. 128 (2007) 243–262.

[30] Balaya, P., Li, H., Kienle, L. & Maier, J., Adv. Funct. Mater. 13 (2003) 621–625.

[31] Badway F., Cosandey F., Pereira N. & Amatucci G.G., J. Electrochem. Soc. 150 (2003) A1318–A1327.

[32] Li, H., Balaya, P. & Maier, J, J. Electrochem. Soc. 151 (2004) A1878–A1885.

[33] Li H., Richter G. & Maier, J., Adv.Mater.15 (2003) 736–739.

[34] Liao, P., MacDonald, B.L., Dunlap, R.A. & Dahn, J.R., Chem.Mater., 20 (2008) 454–461.

[35] . Laruelle,S.et al., J. Electrochem. Soc. 149 (2002) A627–A634.

[36] C.P. Grey et al., Nature Mater., 12 (2013) 1130−1136.

[37] Miyoung Kim et al., Nano Energy, 19 (2016) 234-245

[38] Won-Sub Yoon et al., ACS Appl. Mater. Interfaces, 10 (2018) 29992−29999.

[39] Jamnik J. & Maier J., Phys.Chem.Chem.Phys. 5 (2003) 5215–5220.

[40] Maier, J., .FaradayDiscuss.134 (2007) 51–66.

[41] Zhukovskii, Y.F., Balaya, P., Kotomin, E.A. & Maier, Phys. Rev. Lett. 96 (2006) 058302.

[42] Zhukovskii, Y.F., Balaya, P., Dolle, M., Kotomin, E.A. & Maier, Phys. Rev.B 76 (2007) 235414.

[43] Ponrouch, A., Taberna, P.L., Simon, P. & Palacin, M.R., Electrochim.Acta, 61 (2012) 13–18.

Chapter 2. Effect of PEDOT:PSS Coating on Manganese Oxide Nanowires for Lithium Ion Battery Anodes

2.1. Introduction

Interest on electric vehicles (EVs) and energy storage systems is continuously increasing because of the depletion of fossil fuels and increasing environmental pollution [1,2]. Thus, many researchers have investigated a variety of energy storage devices such as lithium ion batteries (LIBs) [3-5], sodium ion batteries (NIBs) [6-8], and electrochemical capacitors [9]. Three types of anode reactions occur in LIBs: (1) an intercalation reaction, in which lithium ions are inserted to/removed from the host materials during charge–discharge cycles. For example, lithium ions are inserted to/removed from between a graphite lattice [$LiCoO_2 + 6C \leftrightarrow Li_{1-x}CoO_2 + LixC_6$ ($0 < x < 1$)], (2) a reaction resulting from the alloying of Li metal with metal elements such as Sn, Ge, Sb, Zn, In, Bi, and Cd (Li_xM) , and (3) a "conversion" reaction (or redox reaction). Many transition metal oxides react with lithium ions ($MO_x + 2xLi+ + 2xe^- \leftrightarrow M + xLi_2O$) [10].

Many transition metal oxides can be easily prepared with various nanoscale morphologies and structures [11-15]. Moreover, these materials can exhibit even beyond the theoretical capacity calculated based on conversion reaction mechanism [11-13, 16-28]. It is reported that it can be explained by conjugate charge storage reactions which involve space charge layer between lithium salts and metal surface

[27,28], further oxidation of Mn^{2+} to Mn^{4+} in manganese oxides [19] and reversible formation of gel-like polymer[16].

Manganese-based oxides are considered promising anode materials for LIBs due to their high specific capacity, low toxicity, and low cost, and lower operating voltage than that of other conversion reaction-based materials such as Fe-, Co-, and Ni-based oxides [29]. Manganese oxides have various phases such as MnO, Mn_3O_4, MnO_2, and Mn_2O_3 [30]. Among the various morphologies, one-dimensional (1D) manganese oxide nanostructures such as nanowires (NWs) and nanotubes (NTs) have been studied for many energy applications. However, 1D nanostructured Mn_2O_3 has been rarely investigated in spite of its high theoretical capacity (1018 $mAh \cdot g^{-1}$) and many other advantages. 1D nanostructured Mn_2O_3 has advantage on facilitating electrical transport, and also effectively accommodates volume expansion. In addition, it has a short ion diffusion pathway, which enhances rate capability [31]. However, intrinsic low electric conductivity of manganese oxides reduces its electrochemical performance. Thus, many advanced studies have been carried out to overcome these intrinsic problems. For example, Ma et al. doped copper into Mn_2O_3 [32] and Liu et al. coated carbon onto MnO particles [33]. Wang et al. controlled morphology by synthesizing Mn_2O_3 nanoplates [34]. Also, Yang et al. synthesized Ag–Si core–shell nanowall arrays using Ag cores as electron-conducting pathways, which enhanced the stability and conductivity of Si anodes [35].

Herein, we synthesized a new composite of Mn_2O_3 nanowires and Poly(3,4-ethylenedioxythiophene) polystyrene sulfonate (PEDOT:PSS). PEDOT:PSS is a conductive polymer mixture. The PSS part carries a negative charge due to the deprotonated sulfonyl group and the PEDOT part has conjugated rings that carry a

positive charge. PEDOT:PSS has very high conductivity (ca. 300 $S \cdot cm^{-1}$) and high stability [36]. Composite of carbonaceous materials/metal oxides designed to improve the conductivity is usually synthesized in too reductive condition for maintaining structure of metal oxides. However, in our composite of α-Mn_2O_3 nanowires and PEDOT:PSS, α-Mn_2O_3 nanowires maintained its structure by virtue of a mild condition for PEDOT:PSS coating process. The nanosized metal oxides particles agglomerate together to stabilize their surface energy, which lead to poorly dispersed active materials during preparing slurry, while the nanowires is well distributed within the electrode. Thus, keeping the morphology of Mn_2O_3 NWs is important to enhance the electrochemical performance for the lithium ion battery. The PEDOT:PSS coated one-dimensional manganese oxides had improved the electronic conductivity, enhanced stability of the electrochemical active sites.

2.2. Experimental section

2.2.1. Synthesis of α-Mn_2O_3 nanowires

The synthesis method for α-MnO_2 nanowires was similar to the reported hydrothermal method [37]. Then, 7.35 g of $Mn(CH_3COO)_2 \cdot 4H_2O$ (0.03 mol) was dissolved in 80 mL of deionized water in a Teflon container, followed by the addition of 6.85 g of $(NH_4)_2S_2O_8$ (0.03 mol) and 7.94 g of $(NH_4)_2SO_4$ (0.06 mol). After thorough mixing, the solution was heated in an autoclave at 140 °C for 12 h. The resulting α-MnO_2 nanowires were collected by centrifugation and washed three times with water and ethanol. The products were calcinated at 550 °C for 1.5 h.

2.2.2. Coating PEDOT:PSS onto α-Mn_2O_3 nanowires

300 mg of as-prepared α-Mn_2O_3 nanowires were dispersed in a co-solvent (27 mL of water and 270 mL of ethanol) in a round-bottom flask, followed by the addition of 3 mL of PEDOT:PSS solution (CLEVIOS™ P). The mixture was sonicated for 1 h at room temperature. After sonication, we collected the black precipitate by several rinse-centrifugation cycles. The precipitate was fully dried in vacuum for characterization.

2.2.3. Materials characterization

$Mn(CH_3COO)_2 \cdot 4H_2O$, $(NH_4)_2S_2O_8$ and $(NH_4)_2SO_4$ were purchased from SAMCHUN. PEDOT:PSS was purchased from Clevious™. Ethanol was purchased by J.T. Baker. The morphologies of α-Mn_2O_3 nanowires and α-Mn_2O_3/PEDOT:PSS were confirmed by transmission electron microscopy (TEM, Hitachi-7600) and field emission scanning electron microscopy (FESEM, Hitachi S-4300). The crystallographic phase of α-Mn_2O_3 was identified by X-ray diffractometer (XRD, D-MAX2500-PC). The diffraction data was collected in the 2 θ range of 10˚ ~ 80˚. Energy dispersive spectroscopy (EDS) mapping of α-Mn_2O_3/PEDOT:PSS was performed by high-resolution TEM (HRTEM, JEM-2100F, JEOL Ltd.). Thermogravimetric analysis (TGA, SDT-Q600, TA Instruments) and Fourier transform infrared spectroscopy (FT-IR, Nicolet™ iS™10, Thermo scientific) were used to characterize the amount and presence of PEDOT:PSS, respectively. The shift of binding energy was assigned by X-ray photoelectron spectroscopy (XPS, AXIS-HIS, Kratos Inc.). X-ray absorption spectroscopy (XAS) analyses were performed at the 8C beam beamline of the Pohang Light Source (PLS). The cycled electrodes for

XAS analyses were prepared by disassembling of the cells, washing them with diethyl carbonate, and drying them. Finally, the electrodes were sealed with Kapton® tape. All preparation processes were carried out in an argon-filled glove box.

2.2.4. Electrochemical measurements

The working electrode was prepared by coating a slurry containing active material (70 wt%), Super P (as a conductive agent, 20 wt%), and polyvinylidene fluoride (PVDF, 10 wt%) onto copper foil. The coated electrodes were dried under vacuum at 120 °C for 12 h and then pressed. The electrochemical performance of the active material was examined using CR2032 button cells consisting of the as-prepared electrode, a polypropylene separator, lithium foil as the counter electrode, and 1 M $LiPF_6$ in a mixture of ethylene carbonate (EC) and ethyl carbonate (DEC) (v/v = 50:50) as the electrolyte. The cells were assembled in an argon atmosphere glove box. A WBCS3000 cycler (WonA Tech, Korea) was employed for the galvanostatic charge–discharge experiment in a voltage range of 0.01–3 V versus Li^+/Li and for cyclic voltammetry (CV) measurements from 3 to 0.01 V versus Li^+/Li at a scan rate of 0.1 $mV \cdot s^{-1}$ at room temperature. Electrochemical impedance spectroscopy (EIS) was conducted in the frequency range from 100 kHz to 0.01 Hz with an AC signal amplitude of 5 mV (Autolab, PGSTAT128N)

2.3. Results and discussion

2.3.1 Synthesis and characterization of materials

α-MnO_2 nanowires were synthesized through a cation template-assisted hydrothermal method. These α-MnO_2 nanowires transformed into α-Mn_2O_3 at

450 °C or more in air. Fig. 2.1 shows the process of coating PEDOT:PSS onto the α-Mn_2O_3 nanowires. After heat treatment of as-prepared α-Mn_2O_3 nanowires at 550 °C in air, PEDOT:PSS was added to the nanowires via sonication. We obtained α-Mn_2O_3/PEDOT:PSS after 1 h in sonication. The morphology of α-MnO_2 and bare α-Mn_2O_3 nanowires are shown in TEM and SEM images (Fig. 2.2a–c). The prepared α-MnO_2 nanowires have 1D nanostructure with a diameter of 20 nm. The obtained α-Mn_2O_3 nanowires after heat treatment at 550 °C (or higher temperature) maintained their morphology even though the structures are changed. Furthermore, the morphology of α-Mn_2O_3 was still maintained after the coating process. Unlike a carbon-coating process, the PEDOT:PSS-coating process can omit heat treatment at high temperature, which causes morphology change with a phase transition. The mild conditions of the PEDOT:PSS coating process has a significant advantage for applying conductive coatings onto electric materials. The XRD patterns of α-MnO_2 and the α-Mn_2O_3 nanowires were well matched with α-MnO_2 phase (PDF#44-0141) and α-Mn_2O_3 phase (PDF#24-508), respectively (Fig. 2.2d). The existence of PEDOT:PSS was characterized after the coating process by SEM, TEM, and EDS mapping (Fig. 2.3). It is clearly seen that the diameter of α-Mn_2O_3/PEDOT:PSS nanowires is thicker than that of α-Mn_2O_3 nanowires (Fig. 2.3a). In addition, the coating of PEDOT:PSS on α-Mn_2O_3 nanowires is observed in TEM and EDS mapping (Figs. 3b and c). According to TGA, approximately 23% PEDOT:PSS was contained in α-Mn_2O_3/PEDOT:PSS nanowires. Also, the weight of bare α-Mn_2O_3 decreased because of its phase transition from α-Mn_2O_3 to Mn_3O_4, the removal of water from the surface hydroxyls, and the decomposition of a slight amount of SO_4^{2-} species on the surface (Fig. 2.4a)[38]. The surface chemical species of α-

Mn_2O_3/PEDOT:PSS and bare α-Mn_2O_3 were verified by FT-IR. α-Mn_2O_3/PEDOT:PSS exhibited unique peaks of PEDOT:PSS from 3500 to 3000 cm^{-1} and from 1700 to 750 cm^{-1} (Fig. 2.4b) [39]. Peaks indicating SO_4^{2-} anions (1260 to 900 cm^{-1}) and –OH groups from the adsorbed water and surface hydroxyls (~3400 and ~1600 cm^{-1}) were also found [40]. Both spectra showed peaks corresponding to the vibration of the Mn–O bond in Mn_2O_3 [41].

We further analyzed the chemical and oxidation states on surface of both materials by XPS. Binding energy shifts to lower appeared in both Mn 2p and O 1s spectra after coating (Figs. 2.4c and d, respectively). In addition, Messmer et al. reported that the electrostatic contribution affects binding energies [42]. The electrostatic interaction reduced the binding energies of the Mn–O bond in the α-Mn_2O_3 nanowires. After the addition of PEDOT:PSS, the two peaks of Mn 2p shifted to lower binding energy about 0.4 eV (642.4 → 642.0 eV and 654.4 → 654.0 eV, respectively) and the peaks of O 1s shifted 0.4 and 0.1 eV (530.8 → 530.4 eV and 532.2 → 532.1 eV), respectively. These O 1s peaks were caused by the presence of the S–O bond in the SO_4^{2-} anion and the adsorbed water on the surface [43].

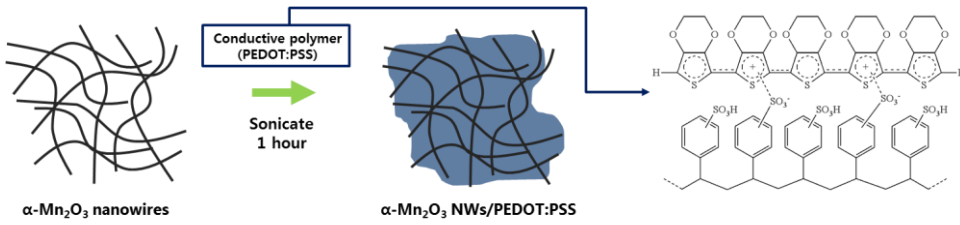

Fig. 2. 1 Schematic representation of the synthesis of α-Mn_2O_3/PEDOT:PSS.

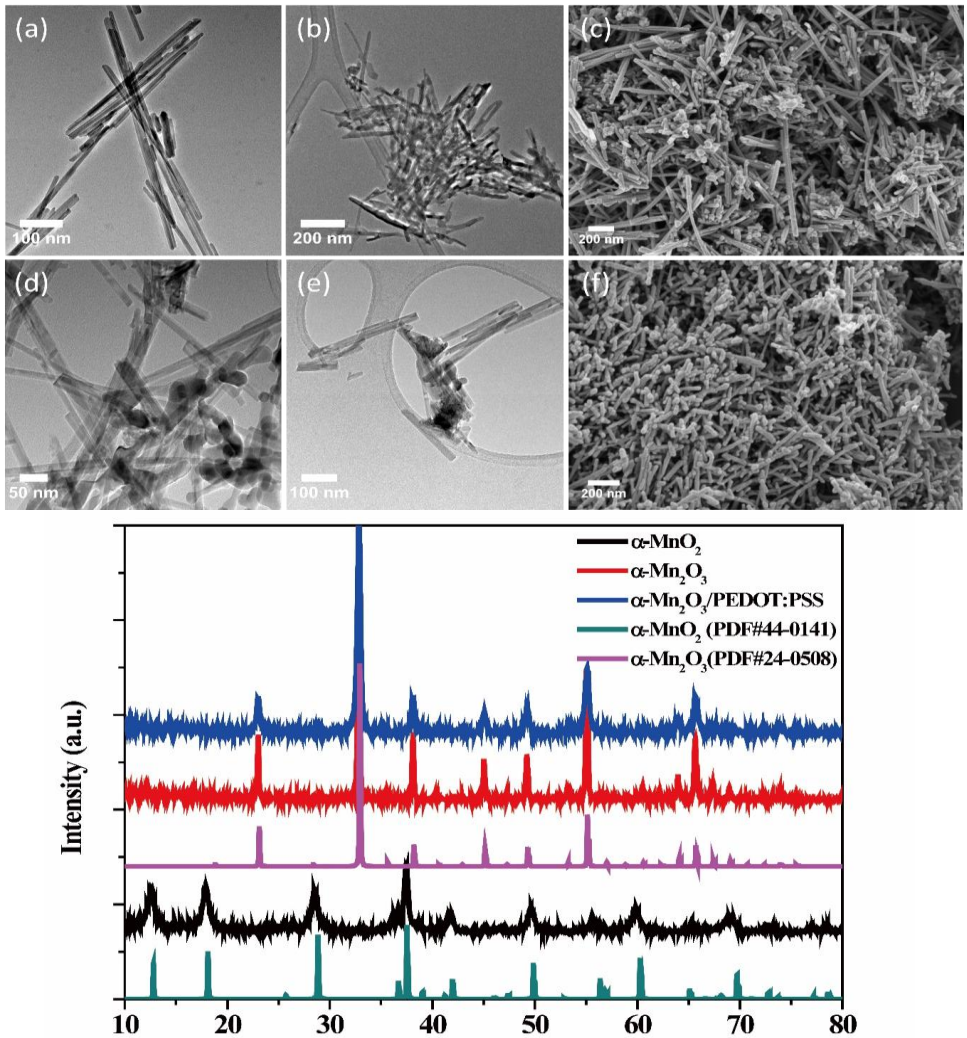

Fig. 2. 2 (a) TEM image of α-MnO_2 nanowires. (b) TEM and (c) SEM images of α-Mn_2O_3 nanowires. (d), (e) TEM and (f) SEM images of α-Mn_2O_3/PEDOT:PSS. (g) XRD patterns of α-MnO_2, bare α-Mn_2O_3 and α-Mn_2O_3/PEDOT:PSS

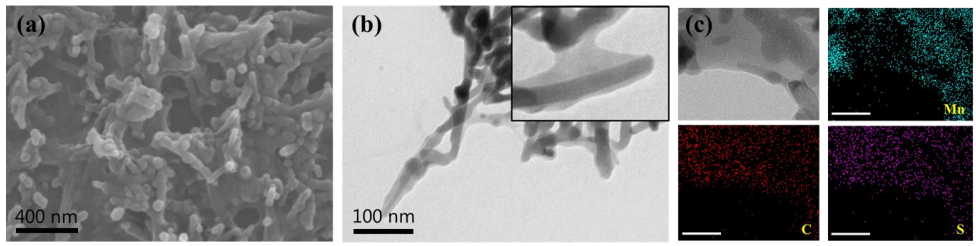

Fig. 2. 3 (a) FE-SEM and (b) TEM image of α-Mn_2O_3/PEDOT:PSS. (c) EDS-mapping of α-Mn_2O_3/PEDOT:PSS. All scale bars in d are 50 nm.

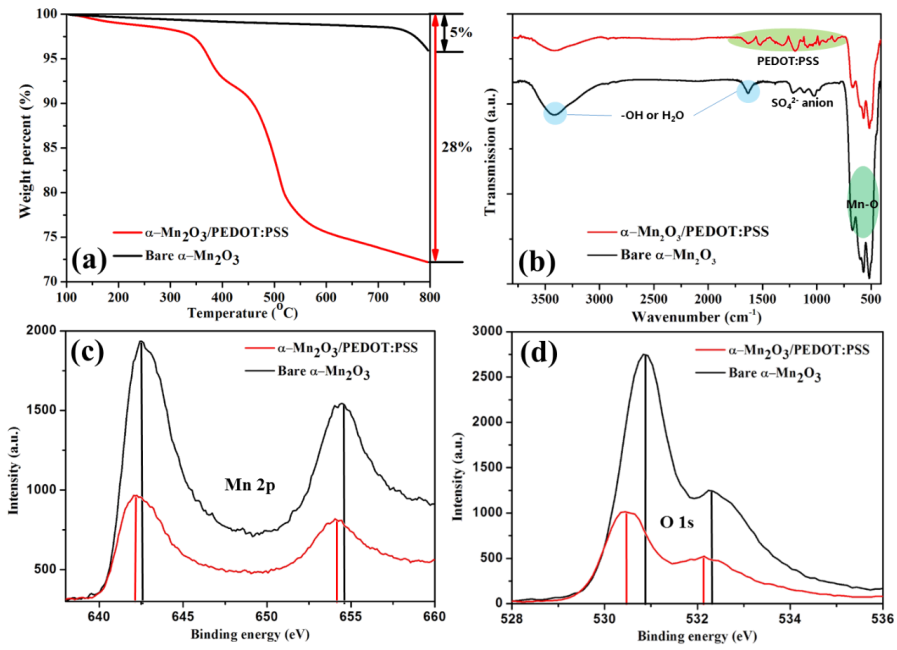

Fig. 2. 4 (a) TG analysis before and after treatment of PEDOT:PSS. (10 ˚C /min, Air condition) (b) FT-IR spectra before and after treatment of PEDOT:PSS. XPS spectra of the (c) Mn and (d) O atoms in materials before and after treatment of PEDOT:PSS.

2.3.2 Electrochemical performance of Mn_2O_3 and Mn_2O_3/PEDOT:PSS

The electrochemical performance was evaluated by galvanostatic charge and discharge measurements. Fig. 2.5a shows the cycle performance of α-Mn_2O_3/PEDOT:PSS and α-Mn_2O_3 at a current density of 100 $mA \cdot g^{-1}$ in a potential range between 0.01 and 3 V. The specific capacities of α-Mn_2O_3/PEDOT:PSS and α-Mn_2O_3 decreased during initial several cycles [23]. However, the capacity of α-Mn_2O_3/PEDOT:PSS gradually increased after 25 cycles. The capacity reached a maximum value of 1450 $mAh \cdot g^{-1}$ after 200 cycles, whereas the capacity of α-Mn_2O_3 still under 400 $mAh \cdot g^{-1}$ after 200 cycles even though the capacity continuously increases after about 40 cycles. At higher current density, fluctuation on cycle performance was also observed. The capacity of α-Mn_2O_3/PEDOT:PSS decreased up to the 50th cycle and then started to rebound at 500 $mA \cdot g^{-1}$. These abnormal trends of increasing capacity after decreasing were further investigated through charge–discharge voltage profiles. Fig. 2.5c and d show the charge and discharge curves of α-Mn_2O_3/PEDOT:PSS and α-Mn_2O_3, respectively. Both α-Mn_2O_3/PEDOT:PSS and α-Mn_2O_3 show the typical lithiation and delithiation profiles of manganese oxide. The first lithiation curves can be explained by dividing it into three distinct regions [44]. The first region was caused by the insertion of lithium ions into Mn_2O_3 to form $LiMn_2O_3$, followed by the diffusion of oxygen and lithium ions out of $LiMn_2O_3$ to form MnO, resulting in two quasi-plateaus above 0.3 V. The second region is an extended plateau near 0.3 V, resulting in the largest charge. The second region is related to the transformation from MnO into Mn metal and Li_2O. Finally, the third region is a sloping voltage below 0.3 V, which can be explained by interfacial insertion (or space charges). In the subsequent delithiation

process, the oxidation of metallic manganese to MnO (not to Mn_2O_3) and the diffusion of lithium ions out of Li_2O occurred, which resulted in a plateau near 1.25 V. In the second lithiation process, the extended plateau near 0.3 V corresponding to the reduction of MnO to Mn^0 shifted to 0.45 V. This indicates that the obstacle of second lithiation is lower than that of the first lithiation as a result of formation of nanoscale metal cluster (< 5 nm) imbedded in Li_2O matrix during the first lithiation [19]. In the lithiation curves of α-Mn_2O_3/PEDOT:PSS, main reaction occurs at plateau (0.45 V), which is related to the transformation of MnO to Mn up to 50 cycles. After 50 cycles, however, the plateau near 0.45 V gradually disappears, whereas the slope below 0.45 V gradually expands. It seems that the reaction in end of lithiation (below 0.45) is related to formation of gel-like polymer which is caused by pulverized nano-metal particles [16]. EIS analysis was introduced to investigate the effect of the PEDOT:PSS coating (Fig. 2.5e). The proposed equivalent circuits are a simplification of the real situation based on several assumptions [45,46]. Although the α-Mn_2O_3/PEDOT:PSS electrode did not perfectly agree with the assumptions, the experimental values were consistent with the calculated data. Fig. 2.5e shows the Nyquist plots of α-Mn_2O_3 after 50 cycles and α-Mn_2O_3/PEDOT:PSS after 50 and 100 cycles. The equivalent circuit is presented in Fig. 2.5e, where R_o indicates ohmic resistance and R_f and C_f indicate the resistance of the SEI film and the capacity of the surface-passivating layer, respectively. The resistance of the charge transfer reaction and the capacitance of the double layer are represented by R_c and C_c, respectively. The values of R_o and R_f for α-Mn_2O_3/PEDOT:PSS (1.02 and 24.77 Ω, respectively) after 50 cycles were lower than the those of α-Mn_2O_3 (2.25 and 84.56 Ω, respectively). Furthermore, R_o and R_f of α-Mn_2O_3/PEDOT:PSS after 100 cycles

displays lower values. This improvement is due to the coating of conductive PEDOT:PSS onto the α-Mn_2O_3 nanowire surface, which provided electron channels and served as a favorable binder agent for electrochemical microstructure reconstruction. However, the R_c value of α-Mn_2O_3 (29.78 Ω) is slightly increased after the coating (38.23 Ω for α-Mn_2O_3/PEDOT:PSS). As shown in Fig. 2.5f, rate performance of α-Mn_2O_3/PEDOT:PSS nanowires is also higher than that of α-Mn_2O_3 nanowires.

The cyclic voltammetry analysis showed detailed information on the electrochemical reaction of PEDOT:PSS. As shown in Figs. 6a and b, two strong cathodic peaks at 0.7 V and 0.25 V are observed in the first lithiation curves, corresponding to irreversible solid electrolyte interphase (SEI) formation and the electrochemical reduction of Mn_2O_3 with Li, respectively [21]. During the first delithiation step, one peak near 1.25 V corresponds to the oxidation of manganese metal. The cathodic peak located at 0.25 V shifted to 0.35 V in the subsequent two scans, resulting from reconstruction which similarly occurred in the galvanostatic charge and discharge voltage profiles [21]. In the CV curves of α-Mn_2O_3/PEDOT:PSS, an obvious cathodic peak at 0.12 V and an anodic peak at 0.55 V might be assigned to the reversible formation of an SEI layer due to PEDOT:PSS; This SEI layer disappeared after 10 cycles [47,48]. Figs. 6b and d show CV curves of α-Mn_2O_3/PEDOT:PSS and α-Mn_2O_3/PEDOT:PSS after 100 cycles, respectively. For α-Mn_2O_3/PEDOT:PSS, there is reaction in the low voltage region as compared to the CV curves of α-Mn_2O_3 and another anodic peak at 2.1 V, which corresponds to the oxidation of Mn^{2+} to Mn^{4+}, which increases with repeating charge and discharge cycles [19,49].

2.3.3 Oxidation states of after 100-cycles Mn_2O_3/PEDOT:PSS

Fig. 2.7a shows the XPS spectrum of Mn 2p for α-Mn_2O_3/PEDOT:PSS after 100 cycles. Two peaks at 643.87 and 655.27 eV are observed, which is characteristic of Mn^{4+} [19]. The X-ray absorption near-edge structure (XANES) spectra of the 10 cycled and 100 cycled α-Mn_2O_3/PEDOT:PSS electrode are shown in Fig. 2.7b, as well as a reference for manganese oxides. The corresponding XANES data are sensitive to the chemical and structural conditions of the material. Considering only the chemical condition, the XANES spectra indicate that the oxidation state of manganese in cycled α-Mn_2O_3/PEDOT:PSS is Mn^{2+} [50]. The oxidation states of both 100 cycled α-Mn_2O_3/PEDOT:PSS and α-Mn_2O_3 nanowires is between +3 and +4. This further oxidation on cycling might contribute to increase capacity during cycling.

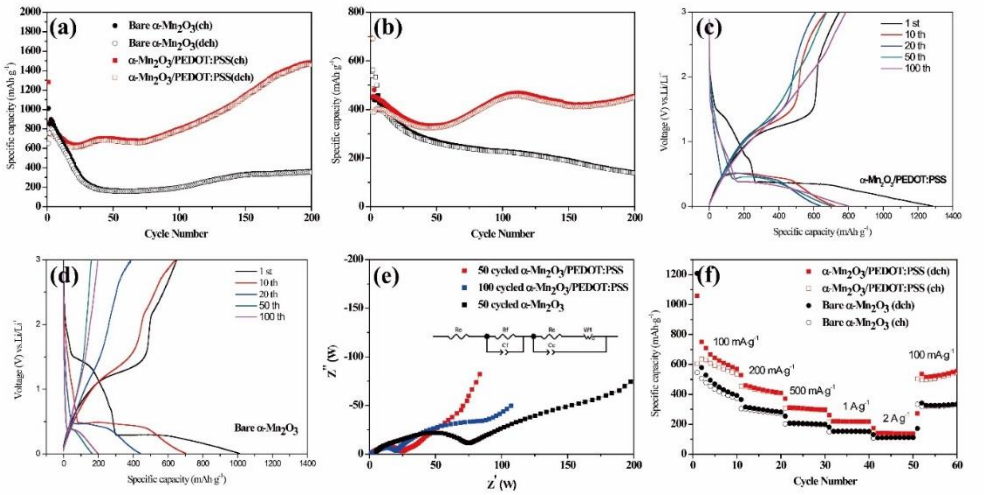

Fig. 2. 5 Cycle performances of bare α-Mn_2O_3 and α-Mn_2O_3/PEDOT:PSS at a current density of (a) 100 mA·g^{-1} and (b) 500 mA·g^{-1}. Voltage profiles of (c) α-Mn_2O_3/PEDOT:PSS and (d) α-Mn_2O_3. (e) AC impedance of α-Mn_2O_3/PEDOT:PSS and α-Mn_2O_3 with equivalent circuit. (f) Rate properties of α-Mn_2O_3/PEDOT:PSS.

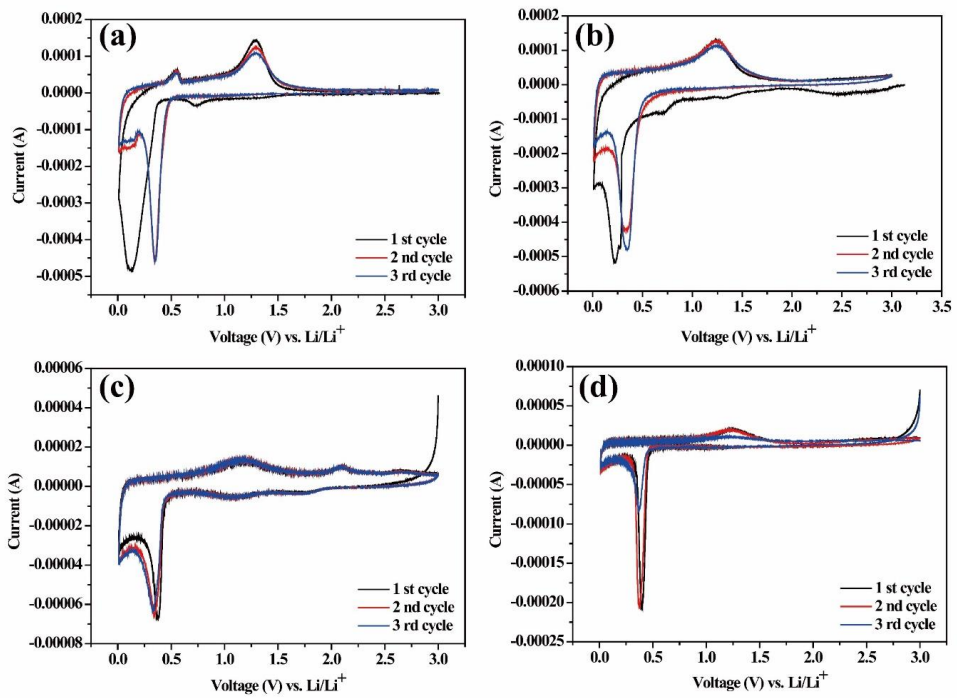

Fig. 2. 6 Cyclic voltammograms of α-Mn_2O_3/PEDOT:PSS (a) during initial 3 cycles and (c) during 3 cycles after 100 cycles at 100mA·g^{-1}. Cyclic voltammograms of bare α-Mn_2O_3 (b) during initial 3 cycles and (d) during 3 cycles after 100 cycles at 100mA·g^{-1}.

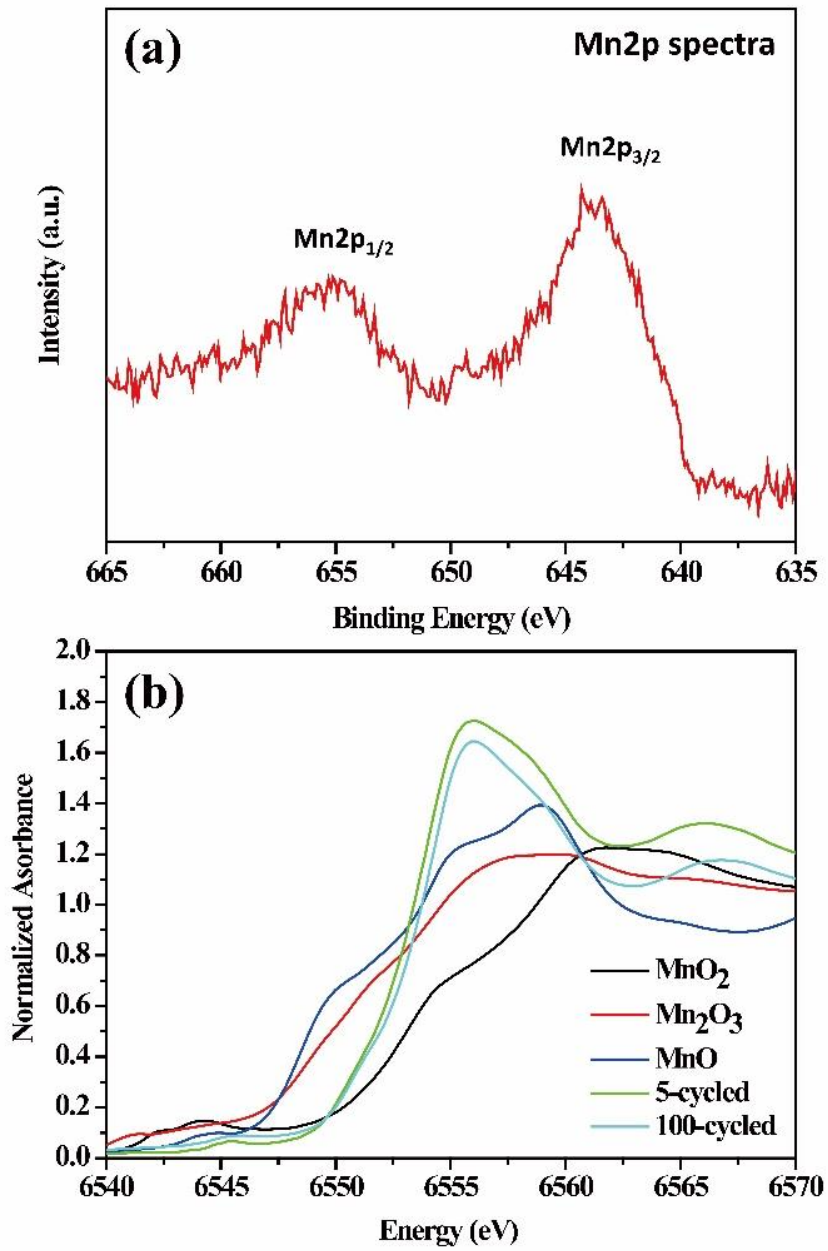

Fig. 2. 7 (a) XPS spectrum of 100 cycled α-Mn_2O_3/PEDOT:PSS at Mn 2p after washing with acetonitrile, (b) normalized Mn K-edge XANES spectrum of α-Mn_2O_3/PEDOT:PSS with reference spectra (MnO_2, Mn_2O_3 and MnO powder).

2.4. Conclusions

We prepared α-Mn_2O_3/PEDOT:PSS nanowires by synthesizing α-MnO_2 nanowire and coating PEDOT:PSS on the as-synthesized α-MnO_2 nanowire followed by heat treatment at 550 °C. α-Mn_2O_3/PEDOT:PSS nanowires showed significantly enhanced electrochemical performance in aspect of cycle stability and rate capability after coating PEDOT:PSS. In addition, α-Mn_2O_3/PEDOT:PSS nanowires exhibited much higher specific capacity than that of bare Mn_2O_3 nanowires and the capacity of Mn_2O_3/PEDOT:PSS nanowires reached about 1450 $mAh \cdot g^{-1}$ after 200 cycles at current density of 100 $mA \cdot g^{-1}$. The abnormal capacity increase on cycling might be due to multiple reasons such as reversible gel-like polymer layer growth on the surface and further oxidation of manganese oxide on cycling.

2.5. References

[1] C. D. Rahn, C.-Y. Wang, Battery Systems Engineering, 1st edn(John Wiley & Sons, Ltd.). 2013.

[2] M. Yoshio, R. J. Brodd, A. Kozawa, Lithium-Ion Batteries-Science and Technologies, 1st edn (Springer). 2009.

[3] H. Li, Z. Wang, L. Chen, X. Huang, Research on Advanced Materials for Li-ion Batteries. Adv. Mater. 21 (2009) 4593-4607.

[4] B. Ellis, K. T. Lee, L. F. Nazar, Positive Electrode Materials for Li-Ion and Li-Batteries. Chem. Mater. 22 (2010) 691-714.

[5] J. B. Goodenough, K. S. Park, The Li-ion rechargeable battery: a perspective. J. Am, Chem. Soc. 135 (2013) 1167-76.

[6] S.-W. Kim, D.-H. Seo, X. Ma, G. Ceder, K. Kang, Electrode Materials for Rechargeable Sodium-Ion Batteries: Potential Alternatives to Current Lithium-Ion Batteries. Adv. Energy Mater. 2 (2012) 710-721.

[7] V. Palomares, P. Serras, I. Villaluenga, K.B. Hueso, J. Carretero-González, T. Rojo, Na-ion batteries, recent advances and present challenges to become low cost energy storage systems, Energy Environ. Sci. 5 (2012) 5884-5901.

[8] H. Pan, Y.-S. Hu, L. Chen, Room-temperature stationary sodium-ion batteries for large-scale electric energy storage, Energy Environ. Sci. 6 (2013) 2338-2360.

[9] G. Wang, L. Zhang, J. Zhang, A review of electrode materials for electrochemical supercapacitors, Chem. Soc. Rev. 41 (2012) 797-828.

[10] V. Etacheri, R. Marom, R. Elazari, G. Salitra, D. Aurbach, Challenges in the development of advanced Li-ion batteries: a review, Energy Environ. Sci. 4 (2011) 3243-3262.

[11] J. Liu, H. Xia, L. Lu, D. Xue, Anisotropic Co_3O_4 porous nanocapsules toward high-capacity Li-ion batteries, J. Mater. Chem. 20 (2010) 1506-1510.

[12] B. Koo, H. Xiong, M.D. Slater, V.B. Prakapenka, M. Balasubramanian, P. Podsiadlo, C.S. Johnson, T. Rajh, E.V. Shevchenko, Hollow iron oxide nanoparticles for application in lithium ion batteries, Nano Lett. 12 (2012) 2429-2435.

[13] X. Wang, X. Li, X. Sun, F. Li, Q. Liu, Q. Wang, D. He, Nanostructured NiO electrode for high rate Li-ion batteries, J. Mater. Chem. 21 (2011) 3571-3573.

[14] M. Laurenti, N. Garino, S. Porro, M. Fontana, C. Gerbaldi, Zinc oxide nanostructures by chemical vapour deposition as anodes for Li-ion batteries, J. Alloys Compd. 640 (2015) 321-326.

[15] M.-S. Park, Y.-M. Kang, G.-X. Wang, S.-X. Dou, H.-K. Liu, The Effect of Morphological Modification on the Electrochemical Properties of SnO_2 Nanomaterials, Adv. Funct. Mater. 18 (2008) 455-461.

[16] S. Laruelle, S. Grugeon, P. Poizot, M. Dollé, L. Dupont, J-M. Tarascon, On the Origin of the Extra Electrochemical Capacity Displayed by MO/Li Cells at Low Potential, J. Electrochem. Soc. 149 (2002) A627-A634.

[17] Y.-Y. Hu, Z. Liu, K.-W. Nam, O. J. Borkiewicz, J. Cheng, X. Hua, M. T. Dunstan, X. Yu, K. M. Wiaderek, L.-S. Du, K. W. Chapman, P. J. Chupas, X.-Q. Yang, C. P. Grey, Origin of additional capacities in metal oxide lithium-ion battery electrodes, Nat. Mater. 12 (2013) 1130–1136

[18] W. Luo, X. Hu, Y. Sun, Y. Huang, Controlled synthesis of mesoporous MnO/C networks by microwave irradiation and their enhanced lithium-storage properties, ACS Appl. Mater. Interfaces 5 (2013) 1997-2003.

[19] Y. Sun, X. Hu, W. Luo, F. Xia, Y. Huang, Reconstruction of Conformal Nanoscale MnO on Graphene as a High-Capacity and Long-Life Anode Material for Lithium Ion Batteries, Adv. Funct. Mater. 23 (2013) 2436-2444.

[20] M. Kundu, C.C. Ng, D.Y. Petrovykh, L. Liu, Nickel foam supported mesoporous MnO_2 nanosheet arrays with superior lithium storage performance, Chem. Commun. 49 (2013) 8459-8461.

[21] X. Li, S. Xiong, J. Li, X. Liang, J. Wang, J. Bai, Y. Qian, MnO@carbon core-shell nanowires as stable high-performance anodes for lithium-ion batteries, Chem. Eur. J. 19 (2013) 11310-11319.

[22] Z. Cai, L. Xu, M. Yan, C. Han, L. He, K.M. Hercule, C. Niu, Z. Yuan, W. Xu, L. Qu, K. Zhao, L. Mai, Manganese oxide/carbon yolk-shell nanorod anodes for high capacity lithium batteries, Nano Lett. 15 (2015) 738-744.

[23] J.-G. Wang, C. Zhang, D. Jin, K. Xie, B. Wei, Synthesis of ultralong MnO/C coaxial nanowires as freestanding anodes for high-performance lithium ion batteries, J. Mater. Chem. A, 3 (2015) 13699-13705.

[24] H. Jiang, Y. Hu, S. Guo, C. Yan, P.S. Lee, C. Li, Rational design of MnO/carbon nanopeapods with internal void space for high-rate and long-life li-ion batteries, ACS Nano 8 (2014) 6038-6046.

[25] Y. Sun, X. Hu, W. Luo, Y. Huang, Porous carbon-modified MnO disks prepared by a microwave-polyol process and their superior lithium-ion storage properties, J. Mater. Chem. 22 (2012) 19190-19195.

[26] Q. Hao, J. Wang, C. Xu, Facile preparation of Mn_3O_4 octahedra and their long-term cycle life as an anode material for Li-ion batteries, J. Mater. Chem. A 2 (2014) 87-93.

[27] H. Li, P. Balaya, J. Maier, Li-Storage via Heterogeneous Reaction in Selected Binary Metal Fluorides and Oxides, J. Electrochem. Soc. 151 (2004) A1878-A1885.

[28] Y.F. Zhukovskii, P. Balaya, E.A. Kotomin, J. Maier, Evidence for Interfacial-Storage Anomaly in Nanocomposites for Lithium Batteries from First-Principles Simulations, Phys. Rev. Lett. 96 (2006) 058302-058304.

[29] Y. Deng, L. Wan, Y. Xie, X. Qin, G. Chen, Recent advances in Mn-based oxides as anode materials for lithium ion batteries, RSC Adv. 4 (2014) 23914-23935.

[30] X. Liu, C. Chen, Y. Zhao, B. Jia, A Review on the Synthesis of Manganese Oxide Nanomaterials and Their Applications on Lithium-Ion Batteries, J. Nanomater. 2013 (2013) 1-7.

[31] L. Mai, X. Tian, X. Xu, L. Chang, L. Xu, Nanowire electrodes for electrochemical energy storage devices, Chem. Rev, 114 (2014) 11828-11862.

[32] Q. Li, L. Yin, Z. Li, X. Wang, Y. Qi, J. Ma, Copper doped hollow structured manganese oxide mesocrystals with controlled phase structure and morphology as anode materials for lithium ion battery with improved electrochemical performance, ACS Appl. Mater. Interfaces 5 (2013) 10975-10984.

[33] X. Wang, S. Qiu, G. Lu, C. He, J. Liu, L. Luan, W. Liu, Fabrication of porous MnO microspheres with carbon coating for lithium ion battery application, CrystEngComm. 16 (2014) 1802-1809.

[34] Y. Zhang, Y. Yan, X. Wang, G. Li, D. Deng, L. Jiang, C. Shu, C. Wang,

Facile synthesis of porous Mn_2O_3 nanoplates and their electrochemical behavior as anode materials for lithium ion batteries, Chem. Eur. J. 20 (2014) 6126-6130.

[35] W. Zhao, N. Du, C. Xiao, H. Wu, H. Zhang, D. Yang, Large-scale synthesis of Ag–Si core–shell nanowall arrays as high-performance anode materials of Li-ion batteries, J. Mater. Chem. A 2 (2014) 13949-13954.

[36] L. Groenendaal, F. Jonas, D. Freitag, H. Pielartzik, J. R. Reynolds, Poly(3,4-ethylenedioxythiophene) and Its Derivatives: Past, Present, and Future. Adv. Mater. 12 (2000**)** 481-494.

[37] X. Wang, Y. Li, Selected-Control Hydrothermal Synthesis of α- and β-MnO_2 Single Crystal Nanowires, J. Am. Chem. Soc. 124 (2002) 2880-2881.

[38] B. Ji, X. Jiao, N. Sui, Y. Duan, D. Chen, Long single-crystalline α-Mn_2O_3 nanowires: facile synthesis and catalytic properties, CrystEngComm 12 (2010) 3229-3234

[39] T.T. Tung, T.Y. Kim, H.W. Lee, E. Kim, T.H. Lee, K.S. Suh, Conducting Nanocomposites Derived from Poly(styrenesulfonate)-Functionalized MWCNT-PSS and PEDOT, J. Electrochem. Soc. 156 (2009) K218-K222.

[40] D. Chen, D. Chen, X. Jiao, Y. Zhao, Hollow-structured hematite particles derived from layered iron (hydro)oxyhydroxide-surfactant composites, J. Mater. Chem. 13 (2003) 2266–2270.

[41] B. Gillot, M. E. Guendouzi, M. Laarj, Particle size effects on the oxidation-reduction behavior of Mn_3O_4 hausmannite, Mater. Chem. Phys. 70 (2001) 54-60.

[42] P. A. Schultz, Shift in XPS levels in ionic adsorbate layers due to electrostatic effects, Surf. Sci. 209 (1989) 229-242.

[43] K. Raj, J.A. Shanmugam, R. Mahalakshmi, R.B. Viswanathan, XPS and IR spectral studies on the structure of phosphate and sulphate modified titania - A combined DFT and experimental study, Indian J. Chem. Sec. A 49 (2010) 9-17.

[44] D. Yonekura, E. Iwama, N. Ota, M. Muramatsu, M. Saito, Y. Orikasa, W. Naoi, K. Naoi, Progress of the conversion reaction of Mn_3O_4 particles as a function of the depth of discharge, Phys. Chem. Chem. Phys. 16 (2014) 6027-6032.

[45] P. Lu, C. Li, E.W. Schneider, S.J. Harris, Chemistry, Impedance, and Morphology Evolution in Solid Electrolyte Interphase Films during Formation in Lithium Ion Batteries, J. Phys. Chem. C 118 (2014) 896-903.

[46] Z. Yang, Y. Feng, Z. Li, S. Sang, Y. Zhou, L. Zeng, An investigation of lithium intercalation into the carbon nanotubes by a.c. impedance, J. Electroanal. Chem. 580 (2005) 340-347.

[47] Z. Chen, J.W.F. To, C. Wang, Z. Lu, N. Liu, A. Chortos, L. Pan, F. Wei, Y. Cui, Z. Bao, A Three-Dimensionally Interconnected Carbon Nanotube-Conducting Polymer Hydrogel Network for High-Performance Flexible Battery Electrodes, Adv. Energy Mater. 4 (2014) 1400207.

[48] Y. Yao, N. Liu, M.T. McDowell, M. Pasta, Y. Cui, Improving the cycling stability of silicon nanowire anodes with conducting polymer coatings,

Energy & Environ Sci. 5 (2012) 7927-7930.

[49] H. Xia, M. Lai, L. Lu, Nanoflaky MnO_2/carbon nanotube nanocomposites as anode materials for lithium-ion batteries, J. Mater. Chem. 20 (2010) 6896-6902.

[50] M.A. Lowe, J. Gao, H.D. Abruña, In operando X-ray studies of the conversion reaction in Mn_3O_4 lithium battery anodes, J. Mater. Chem. A 1 (2013) 2094-2103.

Chapter 3. Structural optimization of peapod-like MnO/C core/shell nanowire via carbonization and effect of carbon shell on the electrochemical performance in lithium ion battery anodes

3.1 Introduction

The Lithium-ion batteries (LIBs) have been a big part of the past 30 years as a power source for portable devices, but it's more demanding in a new, emerging industry such as grid storage, hybrid electric vehicles, and electronic vehicles (EVs) because of their high energy density and long lifespan [1-3]. To meet the demands for the new technical leap in cathodes and anodes, the search for high-performance anode materials is urgent in the next-generation LIBs [2,3]. Transition metal oxide such as iron oxide [4,5], cobalt oxide [6-8], nickel oxide [9], and manganese oxide [10,11] have a higher energy density than graphite and have widely studied as alternative anode materials of LIBs. Manganese oxides, as one kind of transition metal oxides, have a high theoretical specific capacity, can operate at a low conversion potential, and are abundant with low cost and environmental benignity. They are, therefore, appropriate for the electrode materials of LIBs [12]. However, like other transition metal oxides, the intrinsically low conductivity of MnO makes it suffer from poor rate capability. Furthermore, the biggest issue of MnO Materials for LIBs is that they can react with lithium to form metal Mn (dispersed in the Li_2O matrix), resulting in drastic volumetric change and severe capacity fading after only

a few discharge/charge cycles [13,14].

Coating or hybridizing MnO materials with advanced carbon nanomaterials provides an excellent avenue for enhancing the power and energy densities and improving stability. The carbon nanomaterials can significantly enhance the conductivity of MnO, and besides the elastic feature of carbon materials can effectively relieve the strain caused by the volumetric change during lithiation/delithiation process, partly improving their cycling stability. These carbonaceous composite strategies have been demonstrated in the synthesis of MnO/C core/shell nanorods [15,16], MnO NPs attached to graphene [10,11,17] and hollow porous MnO/C microsphere [12,18]. Among them, a peapod-like nanowire with a carbon layer showed excellent performance [20, 23-27]. A peapod-like nanowire structure has advantages such as large surface, internal stress buffered and stable SEI layer formation, and high electron conductivity [23-27]. However, the peapod-like core-shell nanowires reported differed in performance, which seems to depend on the distribution and morphology of the internal oxide particles [25-27]. Therefore, it is essential to not only make a solid structure through carbon coating layer formation but also control the structure of the inner-core oxide particles.

The peapod-like nanowire structures synthesized in the previous study were prepared by heat treatment of the carbon precursor coated nanowire oxides in an inert atmosphere to obtain a carbon coating layer. During the process, oxygen-rich oxides release oxygen and undergo phases changes accompanied by nucleation and particle sintering [20, 23-27]. The equation related to the nucleation rate is proposed as follows [21]:

$$\frac{dN}{dt} = \mathrm{A}\exp\left(-\frac{16\pi\gamma^3 v^2}{3k_B^3 T^3 (lnS)^2}\right)$$

From the equation, three experimental parameters can be variable: supersaturation, temperature, and surface free energy. Supersaturation concentration increases with an increase in the heating rate [21]. Supposing that supersaturation represents the degree of deviation from equilibrium, the equation is applicable even if it is not a solution system.

Sintering is the process that agglomerates fines into a porous mass. The driving force for sintering comes from surface energy [22]. Sintering models include parameters such as particle size, surface area, temperature, time, pressure, and atmosphere.

Structural optimization inner MnO nanoparticles, which was overlooked in the previous studies, was achieved through a controlled carbonization process. Besides, a comparison of the electrochemical performance of the materials synthesized under different conditions was reported.

3.2. Experimental section

All chemicals in this procedure including KMnO4, ethanol, 3,4-dihydroxyphenethylamine (DPA) and 2-amino-2-hydroxymethyl-propane-1,3-diol (TRIS) were A.R. grade reagents used without further purification.

3.2.1 Synthesis of MnOOH nanowires

MnOOH nanowires were prepared by a simple hydrothermal method [28]. 1.0 g KMnO4 was put into a 100 ml Teflon-lined autoclave. The aqueous ethanol solution was prepared by mixing absolute ethanol and distilled water with ethanol volume percent 5%. 40 ml of the aqueous ethanol solution was transferred to the

autoclave. Then, the autoclave was sealed and reacted at 160C for 12 h. The resulting precipitates were filtered and washed with distilled water and dried at 70C for 24 h. The final powders were collected and analyzed characterization.

3.2.2 Synthesis of peapod-like MnO/C

To fabricate carbon modified composite, the peapod-like MnO/C, poly dopamine (poly-DPA) was used as carbon source [29]. Typically, 100 mg of the prepared MnOOH was added into a solution containing 10 mg/ml DPA and 10 mM TRIS. After stirring for 10 minutes, the mixture was stirred continuously for about 6h. Then the resultant precipitate was collected by centrifugation and washing with deionized water, ethanol for several times and dried 70 ^{o}C. Afterward, the as-prepared MnOOH/p-DPA was carbonized under various condition in four different ways to compare each other: 1) Heated to 900 ^{o}C at heating rate of 1 ^{o}C min^{-1} under argon(Ar), 2) Heated to 900 ^{o}C at heating rate of 20 ^{o}C min^{-1} under Ar, 3) Heated to 900 ^{o}C at heating rate of 1 ^{o}C min^{-1} under argon-hydrogen mixed gas(H_2 5v/v%), 4) Heated to 600 ^{o}C at heating rate of 1 ^{o}C min^{-1} under Argon. Table 1 shows samples according to synthesis conditions.

3.2.3 Materials characterization

The morphologies of the peapod-like MnO/C composite were confirmed by transmission electron microscopy (TEM, Hitachi-7600) and field emission scanning electron microscopy (FESEM, Hitachi S-4300). The crystallographic phase was identified by X-ray diffractometer (XRD, D-MAX2500-PC). The *in-situ* XRD data were collected to simultaneously observe the crystallite size of the MnO/C composite

with temperature variation by 1D-detector powder XRD (Xpert PRO, Panalytical). The BET surface area was determined by nitrogen adsorption (BET, ASAP 2010 BET, Micromeritics). Raman spectra were acquired using a Horiba T64000 laser Raman spectrometer. TGA was performed using a TA Instrument SDT-Q600 simultaneous thermal analyzer at a heating rate of 10 ^{o}C min^{-1} in air.

3.2.4 Electrochemical Characterization

The working electrode was prepared by coating a slurry containing active material (70 wt%), Super P (as a conductive agent, 20 wt%), and polyvinylidene fluoride (PVDF, 10 wt%) onto copper foil. The coated electrodes were dried under vacuum at 120 °C for 12 h and then pressed. The electrochemical performance of the active material was examined using CR2032 button cells consisting of the as-prepared electrode, a polypropylene separator, lithium foil as the counter electrode, and 1 M $LiPF_6$ in a mixture of ethylene carbonate (EC) and ethyl carbonate (DEC) (v/v = 50:50) as the electrolyte. The cells were assembled in an argon atmosphere glove box. A WBCS3000 cycler (WonA Tech, Korea) was employed for the galvanostatic charge–discharge experiment in a voltage range of 0.01–3 V versus Li^+/Li and for cyclic voltammetry (CV) measurements from 3 to 0.01 V versus Li^+/Li at a scan rate of 10 or 20 $mV \cdot s^{-1}$ at room temperature.

3.3 Results and discussion

3.3.1 Peapod-like structure formation process

Fig. 3.1 shows the changes in the crystal phase and morphology with temperature in the carbonization process. As shown in Fig. 3.1 (a), the MnOOH nanowire prepared by hydrothermal synthesis has a diameter of 100-150 nm. The diffraction peaks of the MnOOH can be well assigned to MnOOH(JCPDS no. 41-1379, space group $P2_1/c$). As shown in Fig, 1 (b), a coated dopamine layer of approximately 50 to 80 nm is formed on the MnOOH nanowires, and the crystalline phase from the results of XRD does not change from MnOOH even after coating. Dopa-coated MnOOH nanowires were heated at a heating rate of 1 $^oC\ min^{-1}$ in argon. At 300 ^oC, MnOOH phases disappear, and Mn_3O_4 with tetragonal structure (JCPDS no. 24-0734, space group I41/amd) and MnO (JCPDS no. 07-0230, space group Fm3m) are observed. As the phase transformation occurs, numerous small particles are observed, and micropores begin to create. The diffraction peaks of the sample heated to 500 ^oC are sharpened, indicating crystallinity and crystallite size of Mn_3O_4 and MnO increase. At 900 ^oC, particles grow into large spheres and large pores are formed between the particles. The schematic illustration of the formation process of a porous peapod-like core-shell structure was presented in Fig. 3.2 As the phase changes from MnOOH (20.1 $cm^3\ mol_{Mn}^{-1}$) to Mn_3O_4 (15.8 $cm^3\ mol_{Mn}^{-1}$) and MnO (13.1 $cm^3\ mol_{Mn}^{-1}$) in the carbonization process, pores are gradually formed and form a peapod-like structure. Therefore, it is possible to control the MnO particles through adjustment of variables of the carbonization process such as the heating rate, atmosphere, and the temperature [21].

Table 3.1 Details of carbonization process conditions by sample.

Final temperature (°C)	Heating rate (°C min^{-1})	Retention time at final temperature (hr)	Atmosphere	Sample name
900	1	1	Ar	MnO-C900
900	20	1	Ar	MnO-F-C900
900	1	1	H_2	MnO-H_2-C900
600	1	6	Ar	MnO-C600

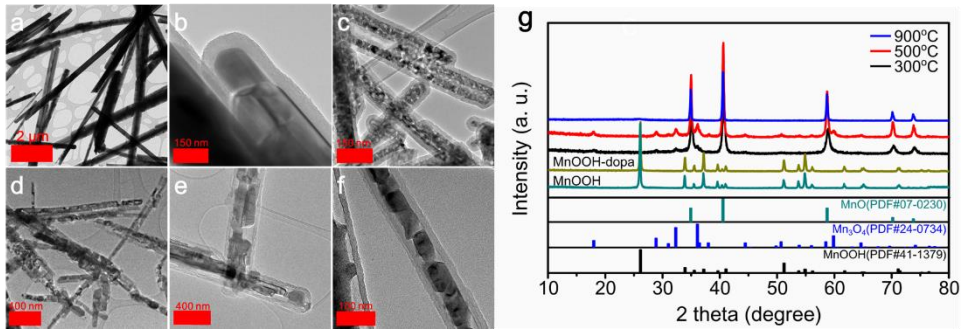

Fig. 3. 1 (a) TEM images of as-prepared MnOOH nanowires, and carbonized dopa-coated MnOOH nanowires depending on temperature (before heating(b), 300 (c), 500 (d) and 900 (e,f) ºC). (g) XRD patterns of as-prepared MnOOH nanowires, and carbonized dopa-coated MnOOH nanowires depending on temperature.

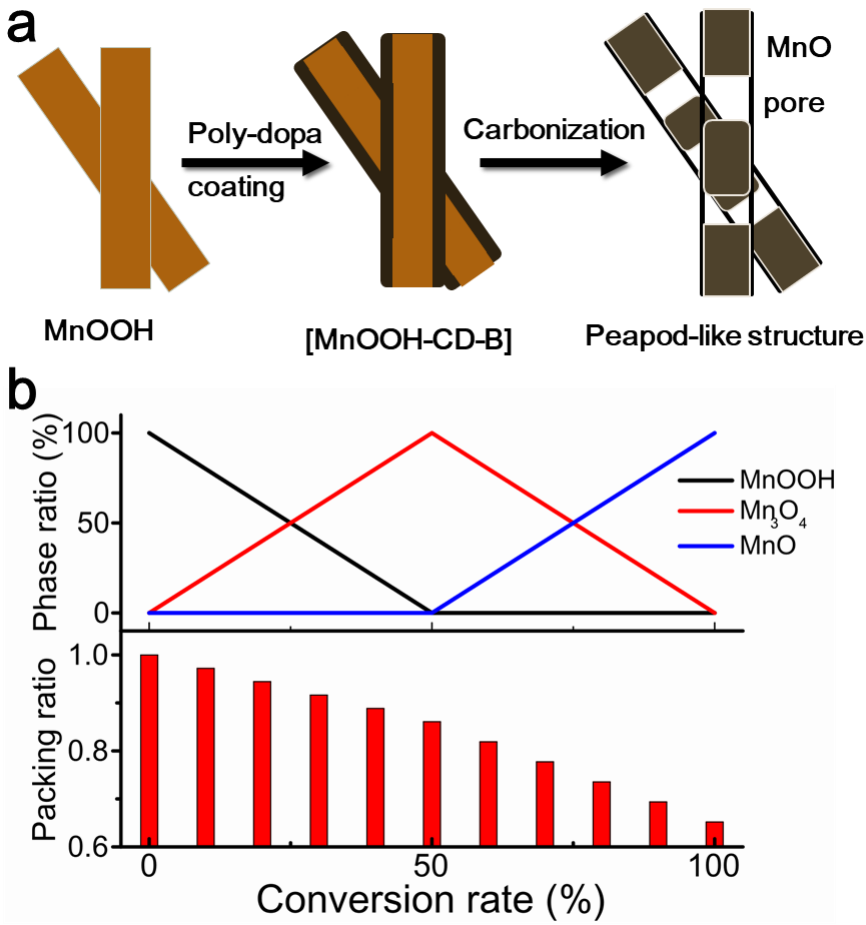

Fig. 3. 2 (a) Schematic illustration of formation process of the peapod-like MnO/C. (b) Plot of phase ratio and packing ratio during transformation from MnOOH, then intermediate product, Mn_3O_4, to final MnO

3.3.2 Characterization of materials synthesized by controlling carbonization process variables

Fig. 3.3 shows the XRD and BET results of peapod-like composites prepared by controlling the carbonization process parameters. The XRD results show that all composites have only MnO phase. Differences in FWHM will be discussed later in the *in-situ* XRD results. The BET surface area of the dopa-coated MnOOH is MnOOH 18.92 m^2 g^{-1}. After the carbonization step, MnO-C600, MnO-C900, MnO-F-C900 and MnO-H2-C900 have values of 123.5, 108.38, 90.53 and 73.93 m^2 g^{-1}, respectively. A comparison of MnO-C900 with MnO-C600 shows the effect of the final temperature. MnO-C600 maintained at a low temperature of 600 ^oC for 6 hours had the largest surface area. The comparison of MnO-C900 with MnO-F-C900 reveals the effect of the heating rate. The BET surface area decreased as the heating rate increased. The comparison of MnO-C900 with MnO-H_2-C900 shows that the surface area decreased in the hydrogen atmosphere.

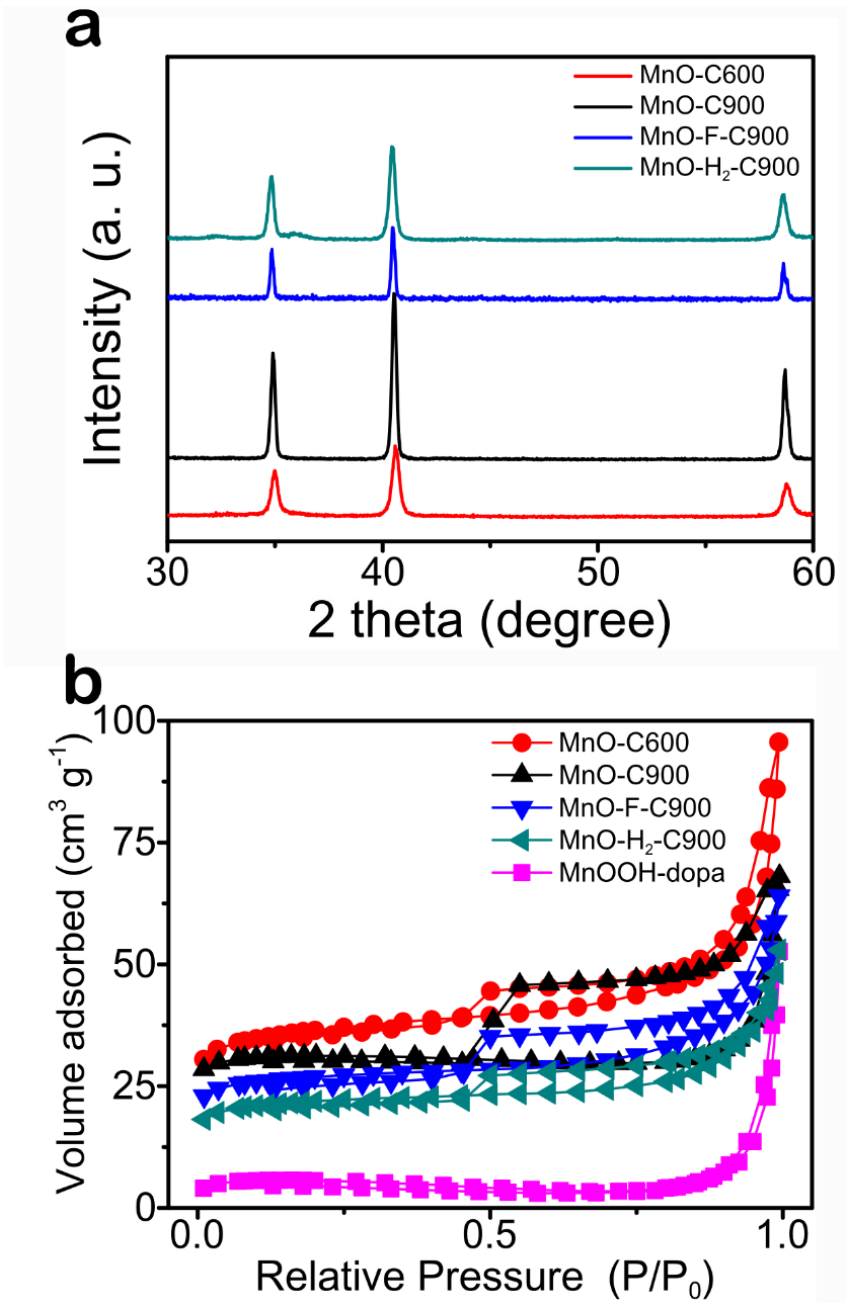

Fig. 3. 3 (a) XRD diffraction patterns and (b) Nitrogen adsorption and desorption isotherms of MnO-C600, MnO-C900, MnO-F-C900 and MnO-H_2-C900.

The *in-situ* XRD results are shown in Fig. 3.4 The atmosphere and furnace operating conditions of the *in-situ* XRD were the same as those of the synthetic furnace. Although the *in-situ* XRD furnace differs in the shape and the flow of the purge gas, the comparison of *in-situ* XRD results seems reasonable. For all samples, the diffraction peaks of MnOOH disappear above 240 ^{o}C. The peak of MnO appears at 340 ^{o}C for MnO-C900 but 340 ^{o}C for MnO-H_2-C900.

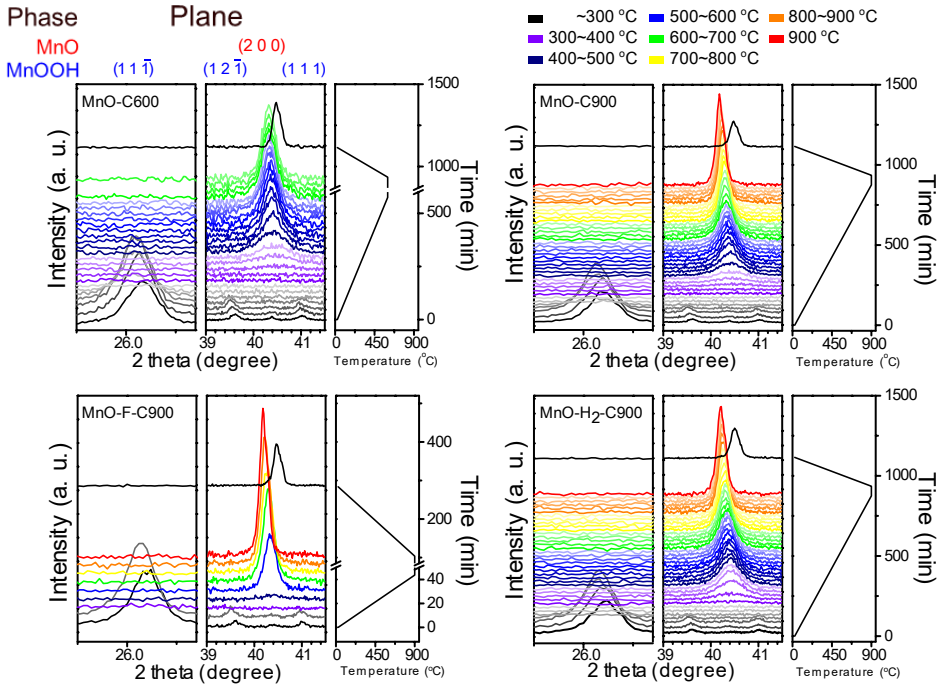

Fig. 3. 4 *in-situ* XRD diffraction patterns of MnO-C600, MnO-C900, MnO-F-C900 and MnO-H_2-C900.

The FWHM of the MnO (200) plane is plotted as a function of time in Fig. 3.5 Other than MnO-F-C900, MnO-F-C900 reached 900 ^{o}C at about 875 minutes due to the 1- ^{o}C min^{-1} heating rate (from 25 ^{o}C), and MnO-F-C900 reached 900 ^{o}C at about 43 minutes due to a heating rate of 20 ^{o}C min^{-1} (from 25 ^{o}C). The FWHM appears to be decreasing rapidly as the temperature rises. In particular, the change in FWHM of MnO-F-C900 is very dramatic. MnO-H_2-C900 exhibits MnO peak at a temperature of 220 ^{o}C, 40 ^{o}C lower than the others, and FWHM is generally high. This is because the surface energy of the manganese oxide is lowered by the hydrogen atmosphere[30], and the smaller particle size is stabilized [31]. In the case of MnO-C600, the reduction of FWHM is insignificant even if it is maintained at 600 ° C for 6 hours. This is because the particle coarsening occurs actively at a high temperature of 900 ° C or higher [32].

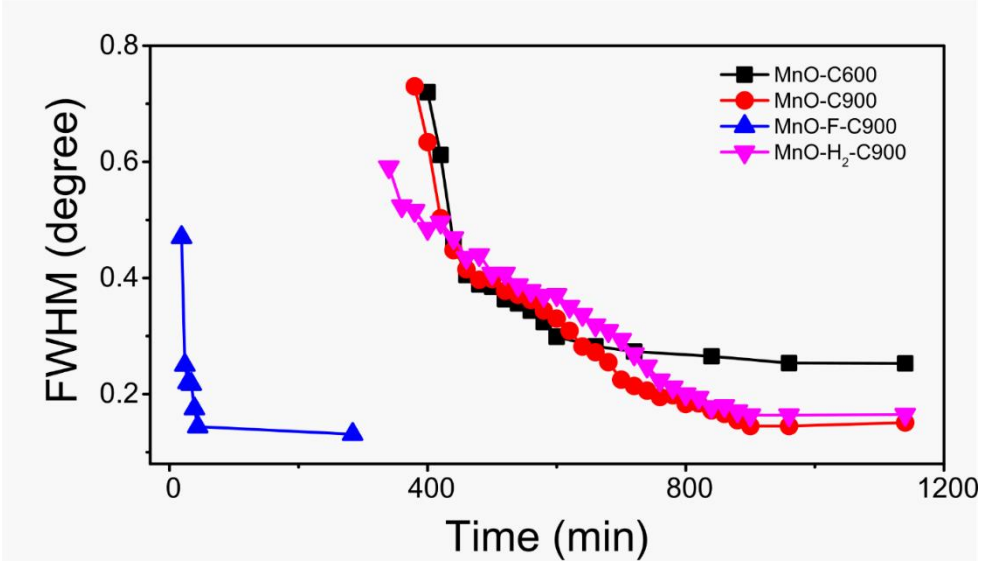

Fig. 3. 5 The full-width-half-maximum FWHM of MnO (200) versus process time obtained from *in-situ* XRD patterns.

TEM images of the four composites are shown in Fig. 3.6. The intergranular space inside MnO-C600 is regular and large. The particles are present in good contact with the carbon coating layer. MnO-C900 has a spherical-like shape which is advantageous for minimizing the surface area, and the particles press and deform the shape of the carbon layer. A high temperature of 900 °C seems to promote the coarsening of the particles [32]. The MnO-F-C900 entangled small particles along the carbon coating layer to form a large porous nanowire. At higher heating rates, the phase formation rate of MnO increases [33]. Consequently, the contact area between neighboring nuclei instantaneously becomes very large, and sintering occurs from the contact surface to grow as porous particles. MnO-H_2-C900 shows a nanowire-like morphology because reductive hydrogen promotes MnO nucleation both inside and outside the surface. The large contact area of small MnO particles activates sintering. Besides, hydrogen than argon is a more favorable environment for the sintering of particles [34].

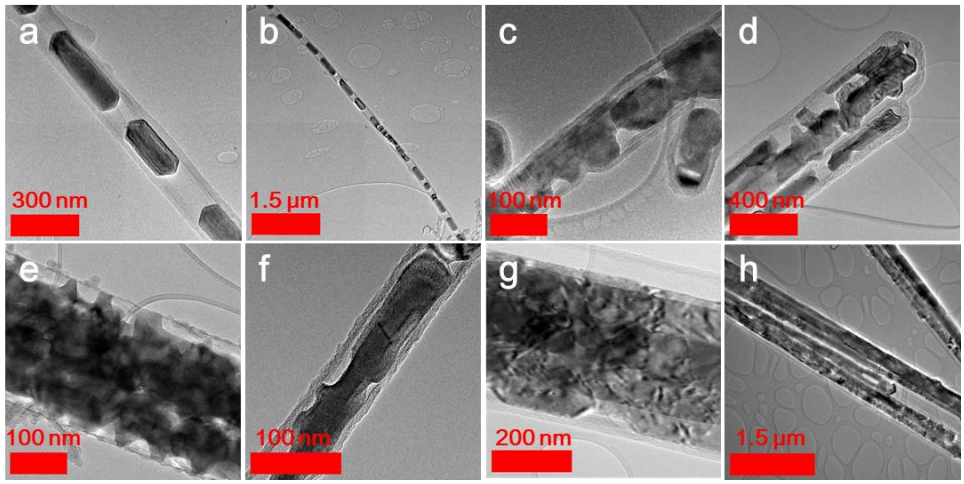

Fig. 3. 6 TEM images of MnO-C600 (a,b), MnO-C900 (c,d), MnO-F-C900 (e,f), MnO-H_2-C900 (g,h).

In order to compare the electrochemical properties between the composites, the charge-discharge cycle experiments were conducted. the charge-discharge cycle experiments were conducted. As shown in Fig. 3.7 (a), all four composites show stable charge-discharge cycle retention. MnO-C600 showed the highest capacity of approximately 1080 mA g^{-1}. The order of capacity after 50 cycles was MnO-C600, MnO-C900, MnO-F-C900, and MnO-H_2-C900. Considering the stress induced by the volume change during the charging-discharging process, the higher inter-particle spatial uniformity that buffered the deformation, the better for the performance.

The voltage profiles of the current density of 100mA g^{-1} are shown in Fig. 3.7 (b). The slope in the range of 1.4-0.4V of the first lithiation curve is observed, corresponding to the lithiation of Mn_3O_4 or Mn_2O_3 which is not observed in XRD results [4, 10, 19]. Since amorphous manganese oxides are easily produced and their oxidation state is higher than the divalent, there may have been higher oxidized manganese oxides that are not present in the XRD results in the composites [35]. The shape and length of the slopes are different in four samples, which implies that the microcrystalline structure of the manganese oxide is greatly influenced by the carbonization conditions. The potential plateau in the range of 0.2-0.55V corresponds to the lithiation process [19]. MnO-C600 exhibits the largest plateau due to the presence of the most electrochemical active MnO.

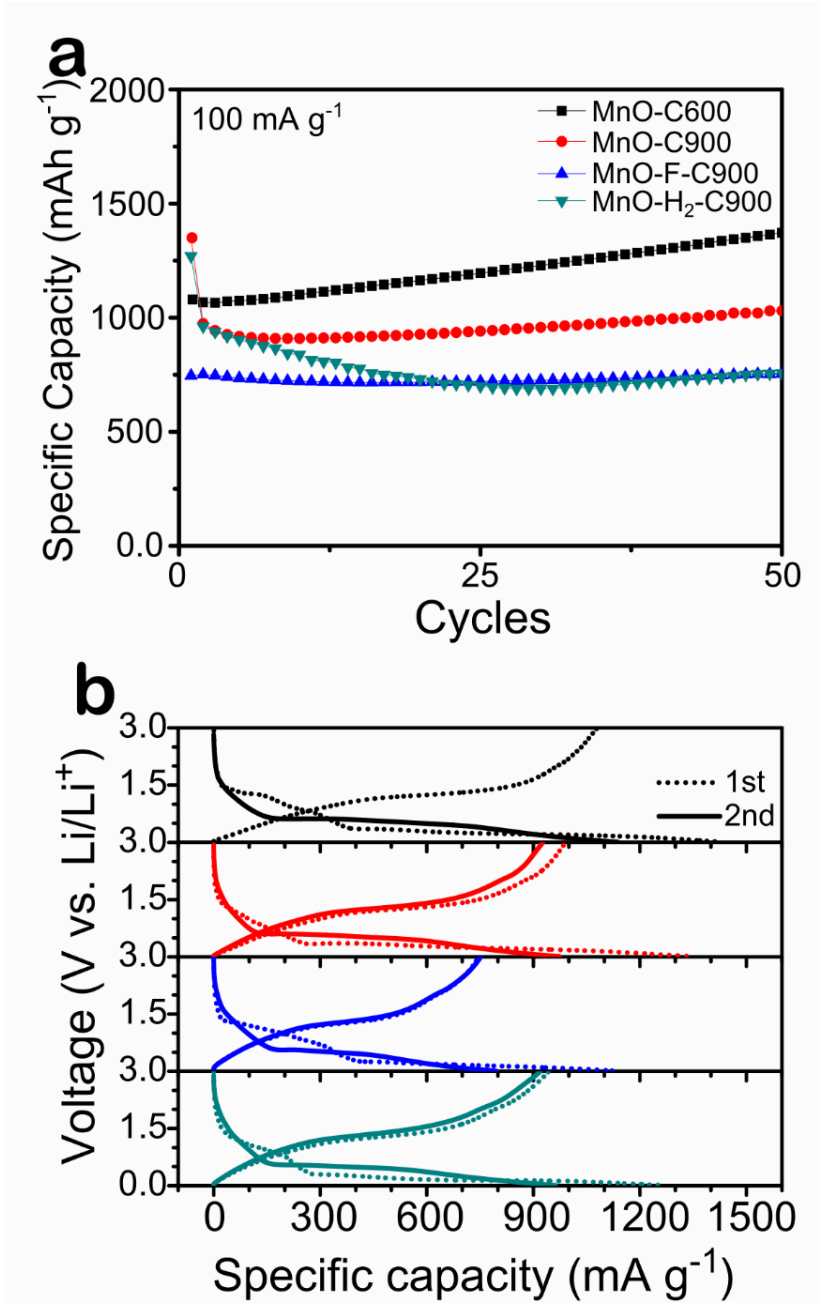

Fig. 3. 7 (a) Cycling performance and (b) Charge-discharge curves of MnO-C600, MnO-C900, MnO-F-C900 and MnO-H_2-C900.

The effect of morphology of particles was further investigated by comparing MnO-C600 and MnO-C900, which showed the highest capacity. Fig. 3.8 (a) shows the cycle performance of MnO-C600 and MnO-C900 at 500 mA g^{-1}. Both samples show excellent cycle retention over 200 cycles. MnO-C900 shows a capacity of about 600 mAh g^{-1} compared to the capacity of 900 mAh g^{-1} at rate of 100 mA g^{-1}. In contrast, MnO-C600 shows a capacity of 800 mAh g^{-1} at 500 mA g^{-1}. Fig. 3.8 (b) shows the rate capability of MnO-C600 and MnO-C900. MnO-C600 shows the average capacities of 1070, 960, 870, 800, 650 and 1070 mAh g^{-1} at current densities of 100, 200, 500, 1000, 2000 and 100 mA g^{-1}, respectively. MnO-C900 shows the capacity of 840, 770, 690, 610, 330 and 830 mAh g^{-1} in the same rate order. The capacities of MnO-C600 shows higher than that of MnO-C900 at all rates. As shown in Fig. 3.8 (c) and (d), both samples show the CV characteristics of a typical MnOx conversion reaction rather than MnO [4, 10, 27]. In the first negative scan process, the peak located at 1.15 V corresponds to reduction of Mn^{4+} to Mn^{2+}, and intense peaks at low potentials at 0.42 and 0.71V are attributed to the reduction of MnO to metallic Mn^0 and the formation of Li_2O [4, 10, 27]. The cathodic peak at 0.75V corresponds to the decomposition of electrolyte and the formation of SEI layer on the surface of electrode materials [25]. In the first positive scan, the peak located at about 1.3 V corresponds to the oxidation of manganese to MnO. For the next scans, only one cathodic peak is observed near 0.42V due to the reduction reaction of MnO to metallic Mn. The peak near 0.21 V of the first scan corresponding to this reaction is shifted by irreversible structural change [19, 25]. Moreover, the cyclic voltammograms of MnO-C600 are overlapped in the second and third scans, implying a highly reversible property.

Fig. 3.8 (e) is the TGA result measured at 10 degrees per minute in the air atmosphere. MnO-C600 and MnO-C900 showed a weight loss of 6.8% and 5.3%, respectively. The weight loss is thought to be the carbon content of each composite material. From the Raman results in Fig. 3.8 (f), two peaks centered at 1350 and 1600 cm^{-1} are observed, corresponding to the D-bond and G-bond of carbon materials, respectively. The I_D/I_G ratios of MnO-600 and MnO-C900 were 0.79 and 0.76, respectively, indicating that the shell is amorphous carbon [36]. The difference in electrochemical performance between MnO-C600 and MnO-C900 may have been caused by the variation in morphology of manganese particles rather than the carbon coating layer.

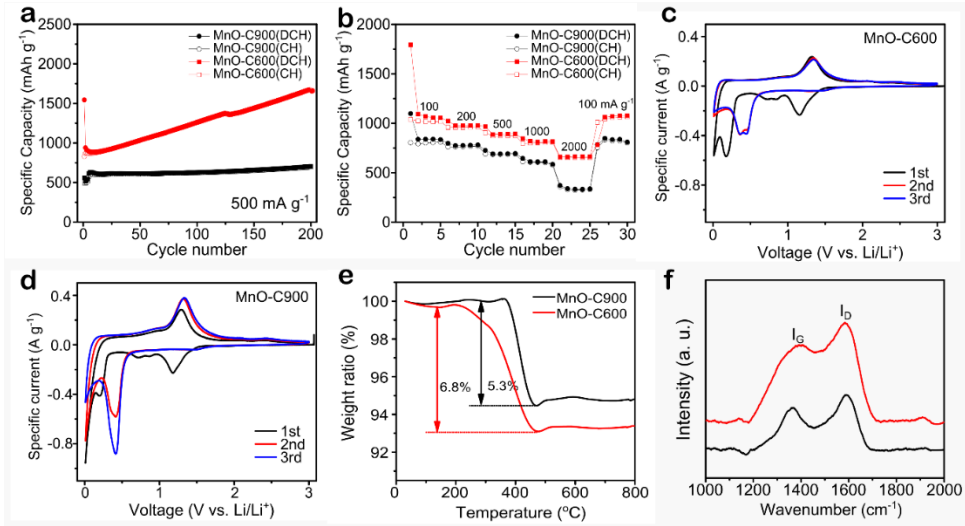

Fig. 3. 8 Cycling performance (a) and rate performance (b) of MnO-C600 and MnO-C900. CVs of MnO-C600 (c) and MnO-C900 (d) at a scan rate of 0.1 mV s^{-1} in the potential range from 3.0 to 0.01 V. (e) TGA curves of MnO-C600 and MnO-C900 under air atmosphere at a rate of 10 °C/min. (d) Raman spectrum for MnO-C600 and MnO-C900.

As shown in Fig. 3.9 (a), the voltage profile of MnO-C600 and MnO-C900 at 500mA g^{-1} was investigated. The potential plateau at 0.2- 0.55 V of the lithiation curve of this voltage profile is referred to as ‘phase II’. The region located in range from 0.55V to 3.0V, before the plateau, is referred to as ‘phase I’ and the region located in range from 0.01V to 0.2V, after the plateau, is referred to as ‘phase III’. ‘phase I’ and ‘phase III’ are the regions where the capacity exhibits due to the reaction in which MnO does not participate [37]. The capacity of ‘phase III’ is due to the "gel-like polymer" or reversible SEI which is not clearly understood but allows a much higher capacity release than the theoretical capacity of the conversion reaction[38]. The capacity of each region and their ratio are shown in Fig. 3.9 (b), (c), (e), and (f). Since ‘phase II’ corresponds to the conversion reaction of MnO, we can trace the change of the amount of electrochemical active MnO by plotting the capacity of ‘phase II’ by cycle number. The capacity of ‘phase II’ in MnO-C900 was 230 mA g^{-1} after 100 cycles and then rapidly decreased to 120 mAh g^{-1} after 200 cycles. On the other hand, the capacity of ‘phase II’ in MnO-C600 exhibited a steady capacity of 550 mAh g^{-1} even after 200 cycles. The cycle test at 500 mA g^{-1} of MnO-C900 shows steady and constant capacity up to 200 cycles, but the capacity release from ‘phase II’ is reduced.

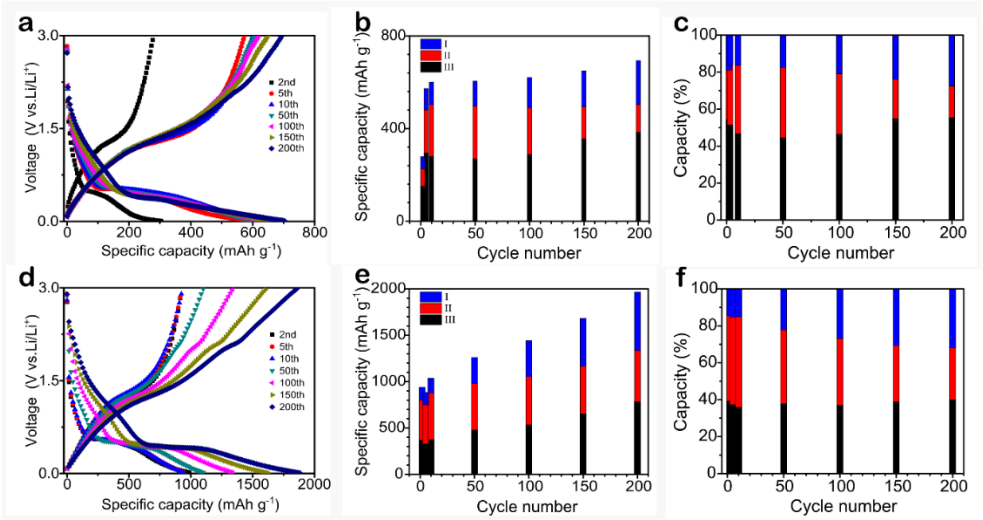

Fig. 3. 9 Electrochemical voltage profile for MnO-C600 (a) and MnO-C900 (d) corresponding to a cycle number at 500 mA g^{-1}. Plot of the discharge capacity of MnO-C600 (b) and MnO-C900 (e) for each region (i.e. insertion I; conversion II; and extra capacity III). Plot of the discharge capacity percent for each process with respect to the total capacity achieved of MnO-C600 (c) and MnO-C900 (f).

TEM images of two composites after 200 cycles at 500mA g^{-1} is provided, which demonstrates the integrity and structural stability of the composites. As shown in Fig. 3.10 (a,b), MnO-C600 has a thick SEI layer on the carbon layer, but the morphology of inner particles remains stable after 200 cycles. On the other hand, as shown in Fig. 3.10 (c,d), the carbon layer of MnO-C900 is demolished and the SEI layer grows thicker on the inner MnO particles. A carbon layer deformed by MnO particles is observed in the TEM image of fresh MnO-C900 shown in Fig. 3.6 (c). The pressed and deformed carbon layer is assumed to be teared down by volume variation during charge and discharge process. The malfunction of the carbon layer fails to prevent agglomeration and disconnection from the electron channel of the MnO particles, and the electrochemical inactive MnO particles seem to accumulate steadily.

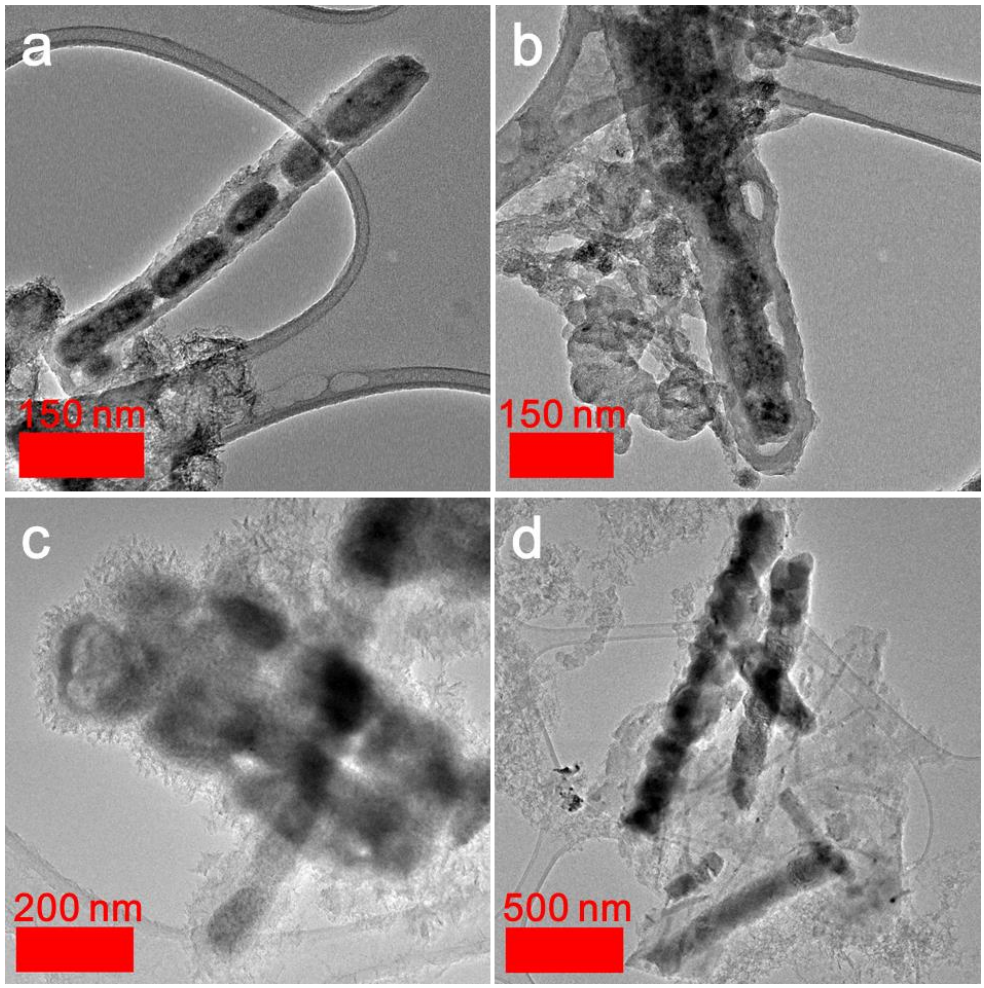

Fig. 3. 10 TEM images of after 200 cycles electrode (@500mA g^{-1}) of MnO-C600 (a,b) and MnO-C900 (c,d).

3.4. Conclusions

In summary, a peapod-like structure with confined MnO particles in the carbon nanotube was synthesized through a carbonization of poly-dopamine covering MnOOH nanowires and the subsequent reduction of the core MnOOH. As MnOOH has a large molar volume, a void space is formed between the MnO nanoparticles during the phase change to MnO, and the morphology and disposition of the MnO nanoparticles in the carbon nanotube are settled. Adjustment of carbonization process parameters converts BET surface area, crystallinity (or crystallite size) and MnO morphology. Although the relationship between electrochemical performance and morphology properties was not clearly demonstrated due to the difficulty of quantifying the morphology properties, a large BET surface area and uniform intergranular spacing appeared to be beneficial for the Li ion storage reaction. Among them, MnO-C600 showed a very stable charge-discharge cycle performance compared to MnO-C900 because the integrity of the structure was maintained due to high stability even in repeated charge and discharge process. Such peapods-like structures with high stability and high power density can be effectively applied to the synthesis of various oxides or carbon composites. The strategy in this study is a promising avenue not only for an anode material for LIBs but also for electrode materials of other energy storage devices.

3.5 References

[1] M.R. Palacin, Chem. Soc. Rev. 38 (2009) 2565.

[2] M. Armand, J.M. Tarascon, Nature 451 (2008) 652-657.

[3] Tarascon, J. M.; Armand, M., Nature 414 (2001) 359−367.

[4] Gu X., Chen L., Ju Z. C., Xu H. Y., Yang J., Qian Y.T. Adv. Funct. Mater. 23 (2013) 4049-4056.

[5] He C.N., Wu S., Zhao N.Q., Shi C.S., Liu E.Z., Li J.J., ACS nano 7 (2013) 4459-4469.

[6] Wang X., Wu X.L., Guo Y.G., Zhong Y.T., Cao X.Q., Ma Y., Yao J.N., Adv. Funct. Mater. 20 (2010) 1680-1686.

[7] Xiao, X. L.; Liu, X. F.; Zhao, H.; Chen, D. F.; Liu, F. Z.; Xiang, J. H.; Hu, Z. B.; Li, Y. D., Adv. Mater. 24 (2012) 5762−5766.

[8] Yan, N.; Hu, L.; Li, Y.; Wang, Y.; Zhong, H.; Hu, X. Y.; Kong, X. K.; Chen, Q. W., J. Phys. Chem. C 116 (2012) 7227− 7235.

[9] Needham, S. A.; Wang, G. X.; Liu, H. K., J. Power Sources 159 (2006) 254−257.

[10] Nam, I.; Kim, N. D.; Kim, G. P.; Park, J.; Yi, J., J. Power Sources 244 (2013) 56−62.

[11] Sun, Y. M.; Hu, X. L.; Luo, W.; Xia, F. F.; Huang, Y. H., Adv. Funct. Mater. 23 (2013) 2436−2444.

[12] Xia, Y.; Xiao, Z.; Dou, X.; Huang, H.; Lu, X. H.; Yan, R. J.; Gan, Y. P.; Zhu, W.

J.; Tu, J. P.; Zhang, W. K.; Tao, X. Y., ACS Nano 7 (2013) 7083−7092.

[13] Goodenough, J. B.; Kim, Chem. Mater. 22 (2010) 587−603.

[14] Jiang, J.; Li, Y. Y.; Liu, J. P.; Huang, X. T.; Yuan, C. Z.; Lou, X. W., Adv. Mater. 24 (2012) 5166−5180.

[15] Sun, B.; Chen, Z. X.; Kim, H. S.; Ahn, H. G.; Wang, X., J.PowerSources 196 (2011) 3346–3349.

[16] Ding, Y. L.; Wu, C. Y.; Yu, H. M.; Xie, J. G.; Cao, S.; Zhu, T. J.; Zhao, X. B.; Zeng, Y. W., Electrochim. Acta 56 (2011) 5844–5848.

[17] Hsieh, C. T.; Lin, C. Y.; Lin, J. Y., Electrochim. Acta 56 (2011) 8861–8867.

[18] Liu, Y. M.; Zhao, X. Y.; Li, F.; Xia, D. G., Electrochim. Acta 56 (2011) 6448–6452.

[19] Michael A.L., Jie Gao, Hector D.A., J. Mater. Chem. A 1 (2013) 2094-2103.

[20] Xingxing Li, Jijiang Fu, Zhihuo Pan, Jianjun Su, Jiangwen Xu, Biao Gao et atl., J. Power Sources 331 (2016) 58-66.

[21] Nguyen T.K. Thanh, N. Maclean, S. Mahiddine,, Chem. Rev. 114 (2014) 7610-7630.

[22] Ashby M.F., Acta Metallurgica, 22 (1974) 275-289.

[23] Xiaowei Li, Shenglin Xiong, Jingfa Li, Xin Liang, Jiazhao Wang, Jing Bai, Yitai Qian Chem. Eur. J. 19 (2013) 11310-11319.

[24] Yu Wang,, Hui Juan Zhang, Li Lu, Ludger Paul Stubbs, Chee Cheong Wong, Jianyi Lin, ACS Nano 4 (2010) 4753-4761.

[25] Hao Jiang,† Yanjie Hu,† Shaojun Guo,‡,* Chaoyi Yan,§ Pooi See Lee,§ and Chunzhong Li†,* ACS Nano 8 (2014) 6038-6046.

[26] Shengbin Wang, Yalan Xing, Changlei Xiao, Huaizhe Xu, Shichao Zhang J. Power Sources, 307 (2016) 11-16.

[27] Zhengyang Cai, Lin Xu, Mengyu Yan, Chunhua Han, Liang He, Kalele Mulonda Hercule, Chaojiang Niu, Zefan Yuan, Wangwang Xu, Longbing Qu, Kangning Zhao, Liqiang Mai Nano Lett. 15 (2015) 738-744.

[28] Weixin Zhang, Zeheng Yanga, Yi Liu, Shupei Tang, Xiaozhao Han, Min Chen, J. Cryt. Growth 263 (2004) 394-399.

[29] Heashin Lee, Shara M. Dellatore., William M. Miller., Philip B. Messersmith, Science 318 (2007) 426-430.

[30] Federico Calle-Vallejo, Marc T.M. Koper, Electrochim Acta 84 (2012) 3-11.

[31] Nancy Birkner, Alexandra Navrotsky, Am. Mineralogist, Volume 97, pages 1291–1298,

[32] Wei Ji, Haiyue Xu, Weimin Wang, Zhengyi Fu, Ceram. Int. 45 (2019) 9363-9367.

[33] Fikri Erdem Şeşen, J. Chem. Tech. App. 1 (2017) 1-2.

[34] A. BOSE, R. M. GERMAN, Metallurgical Transactions A 19A (1988) 2467-2476.

[35] Aparna Iyer, Joselyn Del-Pilar, Cecil K. King'ondu, Edward Kissel, Hector F. Garces, Hui Huang, Abdelhamid M. El-Sawy, Prabir K. Dutta, Steven L. Suib,

J. Phys. Chem. C 11610 (2012) 6474-6483.

[36] J. Schwan, S. Ulrich, V. Batori, and H. Ehrhardt J. Appl. Phys 80 (1996) 440-447.

[37] Bing Sun, Zhixing Chen, Hyun-Soo Kim, Hyojun Ahn, Guoxiu Wang, J. Power Sources, 196 (2011) 3346-3349.

[38] Yan-Yan Hu, Zigeng Liu, Kyung-Wan Nam, Olaf J. Borkiewicz, Jun Cheng, Xiao Hua, Matthew T. Dunstan, Xiqian Yu, Kamila M. Wiaderek, Lin-Shu Du, Karena W. Chapman, Peter J. Chupas, Xiao-Qing Yang, Clare P. Grey, Nature Mater. 12 (2013) 1130–1136.

Chapter 4. Conclusions

The aim of this study is to prepare nanoscale manganese oxide composites coated with conductive materials having structures for effective conversion reaction.

Manganese oxides based on conversion reactions show rapid structural changes during the repeated charge-discharge process. Therefore, the conductive materials coated MnO_x composites such as PEDOT:PSS/Mn_2O_3 and peapod-like MnO@C have been synthesized and demonstrated their improved cycle stability or the structure robust and stable after the repeated charge-discharge cycles. Furthermore, the synthetic methods presented in this study are simple, environmentally friendly, and also make the successful structure for fully exploiting the lithium storage capacity of manganese oxides.

The hydrothermal method was used to obtain uniform nanostructured manganese oxides. The conductive coating layers such as PEDOT:PSS and carbon were added to the synthesized manganese oxides. Especially, in the synthesis of PEDOT:PSS/Mn_2O_3, the conductive coating layer could be formed with the nanowire structure maintained even after the coating process. The coating layer thus synthesized improved the charging-discharging cycle performance of Mn_2O_3 nanowires. It was observed that the oxidation state of manganese increases after the cycle, suggesting that higher utilization of manganese for lithium storage could be achieved via a facile PEDOT:PSS coating process.

Moreover, the peapod-like structure obtained by carbonization of the dopamine coated MnOOH nanowires showed outstanding electrochemical performance. It is noteworthy that control of the parameter of carbonization process allowed control of the morphology of manganese particles in the optimized structure for conversion

reaction. In other words, the optimized structural properties such as higher porosity within the composite and the better dispersed intergranular void space between manganese oxide particles are feasible by adjusting the heating parameter and atmosphere.

To summarize, the manganese oxide composites with conductive coating layer have been constructed using facile processes. The formed coating layer can suppress the structural breakdown which occurs during cycling and improve the cycle stability. The strategy in this study can be further extended for other conversion-based materials, and it is of great potential for next generation energy storage and other applications.

국 문 초 록

리튬 이온 전지는 최근 30년 동안 휴대용 전원으로서 가장 널리 사용되어 소형전자기기 확산에 큰 역할을 하였다. 최근에는 에너지 저장 시스템(ESS)와 전기차와 같은 새로운 시장의 발달로 리튬 이온전지 산업은 새로운 요구에 직면하고 있다. 새로운 시장의 요구에 걸맞게 리튬배터리 연구는 높은 에너지 밀도와 높은 출력과 같은 향상된 특성을 요구를 받고 있다.

전통적인 그라파이트 물질과 비교하여, 컨버전 반응을 하는 전이금속 산화물은 높은 가역용량을 보인다. 하지만 물질의 낮은 전도도와 충방전시의 급격한 부피변화로 인한 용량감소 현상이 나타난다. 지난 20년간 컨버전반응을 위한 연구들은 이러한 문제점을 극복하기 위한 형상제어와 카본기반의 복합물질 개발에 힘써왔다.

먼저 1장 서론에서는 리튬 이온 전지에 대하여 간략하게 소개한다. 리튬 이온 전지의 음극물질을 1) 인터칼레이션 2)합금반응 3) 컨버젼 반응의 3가지 반응메커니즘에 따라 분류하여 설명하였다. 또한 이 장의 마지막에는 컨버전반응에서 나타나는 비이상적 용량발현에 대하여 소개한다.

2장에서는 Mn_2O_3 나노와이어와 Poly(3,4-ethylenedioxythiophene) polystyrene sulfonate (PEDOT:PSS) 로 새로운 전도성 복합체를 합성하였다. Mn_2O_3이 컨버전반응을 하며 충방전사이클이 반복되는 동안 발생하는 용

량감소를 극복하고자 PEDOT:PSS를 첨가하였다. 간단한 초음파 공정을 통해 PEDOT:PSS 가 Mn_2O_3 나노와이어의 구조변형없이 성공적으로 코팅되었다. 코팅된 PEDOT:PSS는 전기적 저항을 줄이고 충방전 동안 망간산화물의 구조가 망가지더라도 전자이동 통로를 확보해 주었다. α-Mn_2O_3/PEDOT:PSS는 100mA g^{-1}전류에서 200사이클후에도 1450 mAh g^{-1}이라는 훌륭한 사이클 성능을 보여주었다. 지속적인 용량증가 현상이 관찰되었는데 이것은 망간표면에서 생성되는 젤-고분자층이 가역적인 반응을 하여 생성되는 것으로 보인다. 결과적으로 PEDOT:PSS 코팅은 충방전으로 인해 발생하는 구조의 붕괴로부터 전자통로를 보호하여 전기화학적 성능을 향상시킨다.

마지막 장에서는 카본화 과정을 통해 콩깍지 구조를 최적화 시키고 그 구조가 전기화학적인 특성에 끼치는 영향에 대하여 연구하였다. 카본화과정 중 발생하는 망간산화물의 상변화가 콩깍지지 구조를 생성하는 요인이었다. 복합체에서 망간산화물의 형상은 1)승온속도 2)분위기 3)최종온도에 따라 달라졌다. 1)승온속도가 높으면 과포화 농도가 증가하고 핵 형성이 촉진되어 짧은 시간에 많은 핵이 생성되며 더 큰 입자가 생성되었다. 2) 수소 분위기 에서는 망간산화물의 계면에너지가 작아져서 핵생성이 촉진되고 치밀화가 빠르게 진행된다. 3) 반면 최종온도가 낮으면 입자성장과 치밀화가 모두 억제되어 큰 입자가 더 커지는 현상이 억제되고 입자가 균일하게 분포된 구조를 얻을 수 있었다. 복합체 내부의 MnO 입자의 형상은 전기화학적 특성에 영향을 끼쳤다. 잘 발달된 기공과 균

일한 입자사이 공간은 전기화학 성능을 향상시켰다. 최적화된 콩깍지 구조는 또한 장기적으로도 매우 안정하고 우수한 전기 화학적 성능을 보였다.

주요어: 리튬 이온 전지, 음극 물질, 컨버전 반응, 망간산화물, 전도성 고분자, 망간산화물/카본 코어쉘

학 번: 2012-30741